Chapter 8

Scalable, Self-Contained Sodium Metal Production Plant for a Hydrogen Fuel Clean Energy Cycle

Alvin G. Stern

Additional information is available at the end of the chapter

http://dx.doi.org/10.5772/67597

Abstract

In this chapter, we present a detailed design study of a novel, scalable, self-contained solar powered electrolytic sodium (Na) metal production plant meant to enable a hydrogen (H_2) fuel, sustainable, closed clean energy cycle. The hydrogen fuel is generated on demand inside a motor vehicle using an efficient hydrogen generation apparatus that safely implements a controlled chemical reaction between either ordinary salinated (sea) or desalinated (fresh) water and sodium metal. The sodium hydroxide (NaOH) byproduct of the hydrogen generating chemical reaction is stored temporarily within the hydrogen generation apparatus and is recovered during motor vehicle refueling to be reprocessed in the self-contained sodium (Na) metal production plant. The electric power for NaOH electrolysis is produced using photovoltaic (PV) device panels spatially arrayed and electrically interconnected on a tower structure that maximizes the use of scarce land area. Our analysis shows that the scalable, self-contained sodium (Na) metal production plant using solar power is technically and economically viable for meeting the hydrogen fuel clean energy needs of all the motor vehicles in the U.S.A. by constructing approximately 450,000 scalable, self-contained sodium (Na) metal production plant units in the southwestern desert region that includes West Texas, New Mexico, Arizona and Southern California.

Keywords: Sodium metal, Sodium metal production plant, Sodium hydroxide, Sodium hydroxide electrolysis, Solar powered electrolysis, Safe hydrogen generation, Hydrogen clean energy cycle

1. Introduction

There is a need in the modern world for sustainable means of producing clean energy economically, on a very large scale. The planet's human population is inexorably increasing toward the 10 billion mark [1–3]. The rapid growth in population presents both opportunities for companies

seeking to broaden markets for their products, and challenges for governments, as the growing populations demand their share of prosperity. It is well known that prosperity generating economic growth requires energy [4–6]. To meet the demands for prosperity, carbon based fossil fuel consumption has increased accordingly, resulting in unacceptable levels of air pollution in major conurbations in both advanced and developing countries [7–10]. Much of the pollution comes from burning fossil fuels inside internal combustion engines (ICEs) of motor vehicles and ships. Coal burning thermal power plants used for electricity generation also contribute substantially to the rise in air pollution [11, 12].

Scientific research has hitherto yielded various solutions to the clean energy challenge using innovative approaches ranging from development of hybrid gasoline-electric motor vehicles (HEVs), plug-in hybrid gasoline-electric motor vehicles (PHEVs), pure battery electric vehicles (BEVs), fuel cell electric vehicles (FCEVs), advanced catalysts for reducing exhaust emissions as well as carbon capture technologies applicable to coal burning thermal power plants [13–17]. These solutions however, work only to mitigate the problem of carbon based fossil fuel emissions and do not address the fundamental problem, namely, how to circumvent carbon based fossil fuels in energy generation and ground transport applications. Although HEV, PHEV, BEV and FCEV technologies offer promise in reducing pollution at least locally, they represent at best, an incomplete remedy to a major problem. HEVs and PHEVs still require combustion of gasoline inside an ICE while BEVs require copious quantities of electrical energy for battery charging, generated by power plants connected to the electric grid. The power plants supplying the electric grid can be hydroelectric or nuclear, but far more often, are fossil fuel burning thermal power plants that are only incrementally more efficient than internal combustion engines in motor vehicles [18]. Since hydroelectric generating capacity in the United States of America (U.S.A.) has already been reached and construction of new nuclear power stations is fraught due to well substantiated fears of radiological leaks, it becomes apparent that the only way to meet the increased demand for electricity from electric vehicle proliferation is by constructing more fossil fuel burning thermal power plants [19, 20].

The FCEVs exist at present in small numbers as vehicle prototypes that function primarily as technology demonstrators [21, 22]. FCEVs are unique however, because they represent the only motor vehicle technology that uses hydrogen (H_2) fuel to generate electric energy to power a motor driving the wheels of the vehicle. Although in existence in various forms since the 1960s, FCEVs have not proliferated for manifold reasons, the principal ones being the absence of means for safely storing hydrogen fuel on board, coupled with a lack of means to economically generate sufficiently pure hydrogen ($H_{2(g)}$) fuel to prevent poisoning sensitive catalysts that might be present in the fuel cells [23, 24]. The existing methods of storing hydrogen on board motor vehicles utilize cryogenic storage of liquid hydrogen ($H_{2(l)}$), storage of hydrogen ($H_{2(g)}$) gas at pressures as high as 70 MPa (10,153 psi) in cylinders made from composite material, and storage as a metal hydride (MH_X) in tanks filled with porous metal sponge or powder comprised of light group 1 and 2 metals and/or transition metal elements, namely, Titanium (Ti) or Nickel (Ni) [25–30]. Such direct hydrogen storage methods however, are impractical due to the high cost of suitable transition metals Ti and Ni, and moreover, because an infrastructure is needed to supply hydrogen directly in large volume to fill liquid or gas tanks or to saturate or replenish the metal sponge within the storage reservoir inside a motor vehicle, a procedure fraught with all of the

http://dx.doi.org/10.5772/67597

well known safety risks associated with handling large volumes of elemental hydrogen [31, 32]. Furthermore, the existing industrial method of generating hydrogen ($H_{2(g)}$) gas using steam reforming of natural gas, the latter containing mostly methane (CH_4), produces significant quantities of carbon monoxide (CO) even after application of the shift reaction, the latter meant to transform the CO into carbon dioxide (CO_2) [33, 34]. The presence of even minute quantities of CO on the parts per million (ppm) order of magnitude in $H_{2(g)}$ fuel, results in rapid poisoning of sensitive platinum (Pt) catalysts present in the latest generation of low operating temperature, proton exchange membrane (PEM) fuel cells [35]. Catalysts based on a mixture of platinum and ruthenium (Pt-Ru) developed to overcome the sensitivity of pure Pt to carbon monoxide poisoning are not cost effective for large scale application in motor vehicle transport applications due to the dearth of ruthenium [36]. Since hydrogen production by conventional steam reforming methods generates significant quantities of CO and CO_2, it becomes difficult to justify using the approach to generate hydrogen (H_2) fuel for FCEVs given that the purpose of advancing such technology is to eliminate carbon based fossil fuel emissions.

Despite challenges, hydrogen (H_2) which is stored in near limitless quantity in seawater is the only alternative fuel that is more abundant and environmentally cleaner with the potential of having a lower cost than nonrenewable carbon based fossil fuels. We have shown in previous published work that a novel apparatus and method for safely generating hydrogen fuel at the time and point of use from ordinary salinated (sea) or desalinated (fresh) water (H_2O) will enable a vehicle range exceeding 300 miles per fueling using direct combustion of the H_2 fuel in appropriately configured internal combustion engines of the Otto or Diesel types, which is comparable to the vehicle ranges presently achieved with gasoline or Diesel fuels, while providing a sustainable, closed clean energy cycle [37]. The novel hydrogen generation apparatus enables hydrogen ($H_{2(g)}$) fuel to be produced on demand in the motor vehicle using a controlled chemical reaction where liquid water ($H_2O_{(l)}$) is made to react with solid sodium ($Na_{(s)}$) metal reactant to produce hydrogen ($H_{2(g)}$) gas and sodium hydroxide ($NaOH_{(s)}$) byproduct according to Eq. (1).

$$2Na_{(s)} + 2H_2O_{(l)} \rightarrow H_{2(g)} + 2NaOH_{(s)} \quad (1)$$

The high purity hydrogen ($H_{2(g)}$) fuel produced on demand by the novel hydrogen generation apparatus can be used to safely power FCEVs without contaminating the sensitive Pt catalysts present in PEM fuel cells or any other types of catalysts in fuel cells, because the hydrogen is not derived from carbon based fossil fuels, and therefore does not contain even trace amounts of carbon monoxide or sulfur compounds. The seawater reactant can be concentrated to as much as 252.18 grams of sea salt solute per kilogram of seawater solution to provide a fusion temperature $T_{Eu} = -21.2$ °C (251.95 K), that is equivalent to the eutectic temperature of a 23.18% by weight NaCl in NaCl-H_2O solution [38, 39]. The concentrated sea salt in seawater solution allows the hydrogen generator to operate reliably over a wide ambient temperature range from –21.2 °C (251.95 K) to 56.7 °C (329.85 K) prevailing in the 48 conterminous states of the U.S.A. [37]. The sodium hydroxide (NaOH) byproduct of the hydrogen generating chemical reaction is stored temporarily within the hydrogen generation apparatus and is recovered during motor vehicle refueling. The NaOH is subsequently reprocessed by electrolysis to recover the sodium (Na) metal for reuse in generating hydrogen fuel.

In this chapter, we describe in detail our company's design approach for constructing a novel, scalable, self-contained electrolytic sodium (Na) metal production plant that uses electric power sourced from the sun. The solar powered electrolytic production plant is meant to form an integral part of a hydrogen fuel, sustainable, closed clean energy cycle in conjunction with the novel, hydrogen generation apparatus, enabling Na metal to be produced cost effectively without negative impact to the environment [37].

2. Sodium metal production plant characteristics

For its successful implementation, the hydrogen fuel, sustainable, closed clean energy cycle requires a means of producing quantities of sodium (Na) metal cost effectively on a large scale by electrolysis of sodium hydroxide (NaOH), the latter created as a byproduct of hydrogen ($H_{2(g)}$) fuel generation inside motor vehicles according to Eq. (1). The electrolysis is performed either on pure sodium hydroxide (NaOH) or on a mixture of NaOH and sea salt, the latter consisting primarily of sodium chloride (NaCl), according to Eqs. (2) and (3) [40–42].

$$4Na^{+} + 4OH^{-} \rightarrow 4Na_{(l)} + 2H_2O_{(g)} + O_{2(g)} \tag{2}$$

$$2Na^{+} + 2Cl^{-} \rightarrow 2Na_{(l)} + Cl_{2(g)} \tag{3}$$

The electrical cost of electrolysis can be estimated from the standard reduction potentials of the oxidation and reduction half reactions that occur at the anode and cathode, respectively of the electrolysis cell when implementing Eqs. (2) and (3) [43].

$$\text{Cathode (reduction):}\ \ Na^{+}_{(aq)} + e^{-} \rightarrow Na_{(s)} \qquad E^{\circ}_{r} = -2.71\ \text{V} \tag{4}$$

$$\text{Anode (oxidation):}\ \ 2Cl^{-}_{(aq)} \rightarrow Cl_{2(g)} + 2e^{-} \qquad E^{\circ}_{o} = -1.36\ \text{V} \tag{5}$$

$$4OH^{-}_{(aq)} \rightarrow O_{2(g)} + 2H_2O + 4e^{-} \qquad E^{\circ}_{o} = -0.40\ \text{V} \tag{6}$$

From Eqs. (4)–(6), the minimum potentials of $E^{\circ}_{ov} = -4.07$ V and $E^{\circ}_{ov} = -3.11$ V are needed to electrolyze NaCl and NaOH, respectively. These voltages are significantly higher than the potential of $E^{\circ}_{ov} = -1.23$ V needed to electrolyze ordinary $H_2O_{(l)}$ to produce $H_{2(g)}$ at the cathode and $O_{2(g)}$ at the anode, however, the benefit from not having to store volatile $H_{2(g)}$ in very large industrial quantities and to transport it between the production plants and refueling stations, outweighs the added electrical cost of producing the solid $Na_{(s)}$ metal.

In the United States of America, the only clean renewable source of energy available in sufficient abundance to implement Eqs. (2) and (3) on a large scale is the radiant energy from the sun that illuminates vast tracts of flat, arid, desert land in West Texas, New Mexico, Arizona and Southern California. The weather in the southwestern U.S.A. is mostly warm and arid with high solar irradiance all year and therefore, constitutes the ideal location for constructing scalable, self-contained solar powered electrolytic sodium (Na) metal production plant units by the thousands [44–48]. Each sodium (Na) metal production plant has to be

http://dx.doi.org/10.5772/67597

capable of operating autonomously as a self-contained factory, requiring minimal maintenance and resources. The diagram showing all of the material and energy inputs and outputs of the self-contained sodium (Na) metal production plant is presented in **Figure 1**.

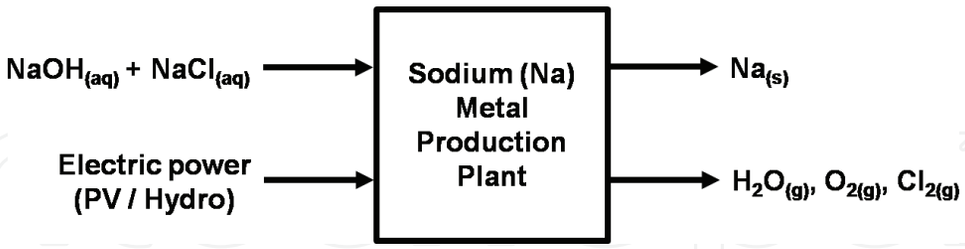

Figure 1. Self-contained sodium (Na) metal production plant operating resources diagram.

In **Figure 1**, electric power for the Na metal production plant is produced using photovoltaic (PV) device panels spatially arrayed and electrically interconnected on a vertical tower structure that maximizes the use of scarce real estate or land area. Up to $N_P = 30{,}000$ PV panels, each having an active area $A_P = 1$ m^2 are mechanically assembled onto the tower, yielding a total PV device panel array active area given as $A_{PA} = N_P \times A_P = (30{,}000$ PV panels$) \times (1$ m$^2) = 30{,}000$ m^2. Sodium hydroxide (NaOH) or a mixture of NaOH and NaCl recovered from motor vehicle hydrogen generators during refueling, must be supplied to the electrolytic cells to replenish the consumed reactants. When operating the hydrogen generation apparatus in warm tropical climates, NaOH exclusively can be recovered from motor vehicle hydrogen generators during refueling because desalinated (fresh) water ($H_2O_{(l)}$) can safely be used as a reactant without risk for it to freeze. Sodium (Na) metal is produced at the electrolytic cell cathode, and steam ($H_2O_{(g)}$), oxygen ($O_{2(g)}$) gas and some chlorine ($Cl_{2(g)}$) gas are produced at the cell anode, the latter resulting from electrolysis of the NaCl in sea salt. The $H_2O_{(g)}$ and $O_{2(g)}$ can be released directly to the atmosphere while the $Cl_{2(g)}$ must be collected, condensed to a liquid and stored in bottles, for subsequent sale to customers that consume chlorine including the paper and polymer (plastic) manufacturing industries [49]. It is also possible to collect and condense the steam generated at the anode and use the liquid water ($H_2O_{(l)}$) for crop irrigation in arid, desert environments where water resources are limited. The layout of the self-contained sodium (Na) metal production plant is shown in **Figure 2**.

The self-contained sodium (Na) metal production plant shown in **Figure 2**, consists of a solar tower that comprises a photovoltaic (PV) device panel array active area given as $A_{PA} = 30{,}000$ m^2. It also consists of a prefabricated Quonset or Q-type metal building having a semicircular cross section, assembled onto a concrete pad foundation that houses electrical switch gear, voltage step down DC-DC converters, the sodium hydroxide (NaOH) electrolytic cells, sodium (Na) metal packaging unit and chlorine (Cl_2) gas separation and bottling unit. A control room permits monitoring the operation of the plant. Two above ground storage tanks are shown located outside of the Q-type metal building with one on either side, for storing aqueous sodium hydroxide ($NaOH_{(aq)}$) solution. Each above ground storage reservoir has a liquid volume capacity of $V_{NaOH(aq)} = 37{,}850$ L (10,000 Gal), and is used to replenish the NaOH in the electrolytic cells after the reactant in the cells has been consumed by electrolysis.

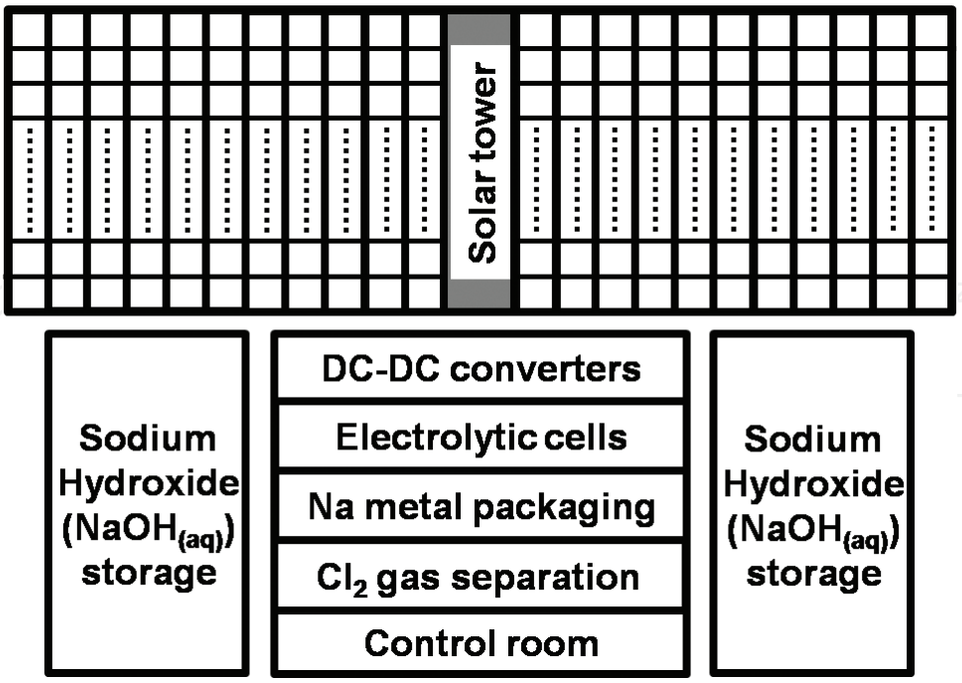

Figure 2. Layout of the self-contained sodium (Na) metal production plant (NOT TO SCALE).

Many factors influence the production yield of sodium (Na) metal during a normal day of plant operation. The two most important factors include the power conversion efficiency of the PV device panels and the magnitude and duration of solar irradiance incident on the PV panels. Other factors affecting the Na metal yield include the power conversion efficiency of the voltage step down DC-DC converter and the efficiency of the electrolytic cell in recovering the Na metal from fused $NaOH_{(l)}$ or from a mixture of fused $NaOH_{(l)}$ and $NaCl_{(l)}$. The efficiency of the voltage step down DC-DC converter depends mainly on how much power is dissipated or lost in the solid state transistors as a result of high frequency on-off switching. The efficiency of the electrolytic cell in this work is viewed in terms of the number of electrons from the electrolytic cell current I_{CELL}, flowing through an electrolytic cell actually needed to produce an atom of Na metal. An alternate definition of the electrolytic cell efficiency might consider the theoretical electric power required to be supplied to the electrolytic cell to produce one mole of Na metal as calculated from the known Gibbs free energy of $NaOH_{(l)}$, divided by the actual power required to be supplied to the electrolytic cell to produce one mole of the Na metal, a definition that we do not consider here. Ideally, each electron flowing through the electric circuit comprising the electrolytic cell should produce one atom of Na metal. In the analysis that follows, it will be assumed that the voltage step down DC-DC converters and the electrolytic cells have efficiencies $\eta_{DC\text{-}DC} = 100\%$ and $\eta_{CELL} = 100\%$, respectively.

2.1. Scalable photovoltaic tower concept

The solar tower comprising the photovoltaic (PV) device panel array supplies electric power to the sodium (Na) metal producing electrolytic cells. The amount of electric energy supplied by the solar tower is a key determinant of the quantity of Na metal that can be electrochemically

http://dx.doi.org/10.5772/67597

separated from the NaOH reactant. The energy conversion efficiency of the photovoltaic (PV) device panels is therefore a critical parameter for determining the amount of Na metal that can be produced by the self-contained sodium (Na) metal production plant. Ideally, the photovoltaic (PV) device panels of the solar tower should have maximum optical to electric energy conversion efficiency approaching the thermodynamic limit $\eta_{PVmax} = 93\%$ [50, 51]. According to the Shockley-Queisser theory, such a high conversion efficiency requires PV devices comprising manifold semiconductor junctions [52, 50]. Contemporary, commercially available single junction, monocrystalline silicon photovoltaic (PV) devices attain energy conversion efficiencies ranging between $\eta_{PV} = 15–18\%$ for front-illuminated silicon devices and up to $\eta_{PV} = 21.5\%$ for back-illuminated silicon devices as summarized in **Table 1**.

	PV panel technology	PV panel area (m^2)	Module efficiency (%)	V_{OC} (V)	V_{MPP} (V)	I_{MPP} (A)	I_{SC} (A)
Sunpower SPR-X21-345	Monocrystalline Si	1.63	21.5	68.2	57.3	6.02	6.39
Suntech STP290S-20	Monocrystalline Si	1.63	17.8	39.8	31.7	9.15	9.55
LG LG280S1C-B3	Monocrystalline Si	1.64	17.1	38.8	31.9	8.78	9.33
First Solar FS-4117-2	Thin film CdTe	0.72	16.3	88.2	71.2	1.65	1.79
Sharp NU-U240F2	Monocrystalline Si	1.63	14.7	37.4	30.1	7.98	8.65

[a]PV panel performance data sourced from respective product datasheets. ASTM AM 1.5G solar irradiance of 1000 W/m^2.

Table 1. Performance of commercial PV device panels in 2016[a].

In **Table 1**, the PV device panels from the Sunpower manufacturing company stand out as having the highest efficiency, due to the use of back-illumination of the silicon device layer. Multijunction devices that offer higher efficiencies remain at a research and development stage and have not reached a level of maturity or cost effectiveness to be ready for release as commercial PV panel products [53]. Our company, AG STERN, LLC is researching the development of advanced, high efficiency PV devices based on novel, very high transmittance, back-illuminated, silicon-on-sapphire semiconductor substrates expected capable of transmitting 93.7% of the total solar irradiance into the semiconductor device layer and therefore capable of achieving an energy conversion efficiency $\eta_{PV} = 90\%$ with proper engineering of the semiconductor photon absorbing layers and PV device structure [54–57].

The solar tower providing power to the electrolytic cells must be scalable in electric power output, and thus capable of allowing PV device panels to be replaced as higher efficiency ones become available, without affecting the overall operation of the self-contained Na metal production plant in any way, other than increasing the Na metal yield. Since the highest performing PV device panels currently offered commercially are listed in **Table 1**, it is possible to calculate the expected power output of the solar tower comprising a PV device panel array active area of $A_{PA} = 30{,}000$ m^2, under ASTM direct normal air mass (AM) 1.5D standard terrestrial solar spectral irradiance with a total irradiance $Irr_{AM1.5D} = 887$ W/m^2, as a function of the PV device efficiency, as shown in **Figure 3**.

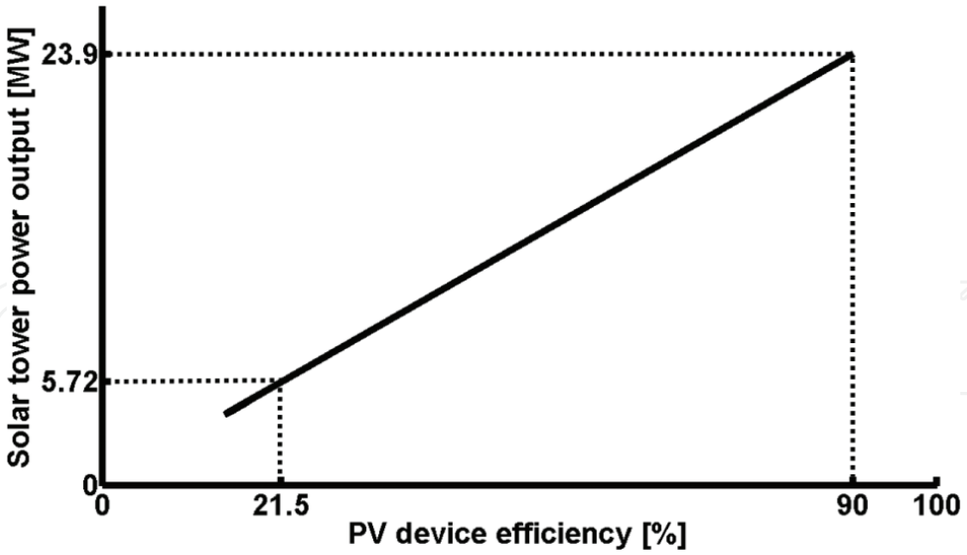

Figure 3. Electric power output for a solar tower PV device panel array with area $A_{PA} = 30{,}000\ m^2$ under ASTM direct normal AM 1.5D standard terrestrial solar spectral irradiance as a function of the PV device efficiency.

It is clear in **Figure 3**, that single junction, monocrystalline silicon PV devices having an efficiency $\eta_{PV} = 21.5\%$ can be arrayed to generate electric power given as $P_{ST} = 5.72$ MW for electrolysis. Once $\eta_{PV} = 90\%$ efficient PV device panels will become available, the electric power output can be increased to a substantial $P_{ST} = 23.9$ MW, entailing that just 50 of the self-contained sodium (Na) metal production plants can generate peak power given as $P_{ST\text{-}50} = 50 \times 23.9$ MW $= 1195$ MW, matching the power generating capacity of a large commercial nuclear power station.

2.2. Solar irradiance conditions

The electric power output of the solar tower comprising photovoltaic (PV) device panels depends on the magnitude and duration of solar irradiance incident on the PV panels, in addition to the PV device energy conversion efficiency described in Section 2.1. It can be assumed that the PV device energy conversion efficiency is constant and might only decrease in value slowly over time [58]. In contrast, the solar irradiance incident on the PV device panels can vary on a daily basis and is determined by two principal factors, namely, the solar geometry and prevailing atmospheric or meteorological conditions.

The sun is effectively a large hydrogen (H_2) fusion reactor, spherical in shape with a radius $R_{sun} = 6.96 \times 10^8$ m located at a mean distance from the earth given as $r_{sun\text{-}m} = 1.496 \times 10^{11}$ m [59, 60]. The total power output of the sun is given as $P_{sun} = 3.8 \times 10^{26}$ W that radiates isotropically in all directions, resulting in a surface temperature of the solar black body $T_{sun} = 5800$ K. Of the total solar power output, earth receives only $P_{earth} = 1.7 \times 10^{17}$ W which if converted to electric power, vastly exceeds the earth's energy needs [61]. The sun therefore constitutes an excellent potential source of clean radiant energy to be harnessed on earth.

The solar geometry has a key role in determining how much radiant energy from the sun will be incident on the PV devices located on earth. To understand how the solar geometry

http://dx.doi.org/10.5772/67597

influences the solar irradiance at the earth's surface, it will be assumed that earth follows a stable elliptical orbit around the sun described by Eq. (7) [59].

$$r_{\text{sun}}(\theta) = \frac{a(1-e^2)}{1+e\cdot\cos(\theta)} \tag{7}$$

$$\text{Perihelion: } r_{\text{sun}}(0^{\circ}) = a(1-e)$$

$$\text{Aphelion: } r_{\text{sun}}(180^{\circ}) = a(1+e)$$

In Eq. (7), the distance r_{sun}, represents the distance from the center of the sun to the center of the earth and the angle θ, represents the angle between the present position of the earth in orbit around the sun, and the perihelion position when it is closest to the sun. The eccentricity $e = 0.01673$, describes the shape of the elliptical orbit of the earth around the sun and the value a, represents the length of the semi-major axis of the orbit defined as the mean distance from the center of the sun to the center of the earth given as $a = \{r_{\text{sun}}(0°) + r_{\text{sun}}(180°)\} / 2 = r_{\text{sun-m}} = 1.496 \times 10^{11}$ m. The period of earth's elliptical rotation around the sun is approximately $T_{\text{es}} = 365.24$ days and the period of rotation around its own axis is approximately $T_{\text{ea}} = 86{,}400$ seconds or 24 hours, the latter known as a *mean solar day* [62–66]. The earth's angular velocity about its own axis is given as $\omega_{\text{ea}} = 7.292115 \times 10^{-5}$ rad/sec, although the rotation is slowing over time [67]. The obliquity or tilt of the earth's axis of rotation with respect to a line perpendicular to the plane of its elliptical orbit around the sun is given as $\varepsilon = 23.44°$, although slight precession and nutation of the axis exists [60]. The *plane of the sun* passes through the center of the sun and remains parallel to the earth's *equator* during the elliptical orbit. The *summer and winter solstices* occur approximately on June 21 and December 21, respectively. The *spring and fall equinoxes* occur approximately on March 21 and September 21, respectively, and are characterized by the length of day being equal to the length of night and the earth's equator coinciding with the *plane of the sun*.

The solar declination angle δ, is the angle made by a ray of the sun (passing through the center of the earth and the center of the sun), and the equatorial plane of the earth. The solar declination angle has a range given as $-23.44° \le \delta \le +23.44°$. On the *summer solstice* day when $\delta = +23.44°$, the sun shines most directly on the earth's latitude $\varphi_{\text{T-CAN}} = +23.44°$, known as the *Tropic of Cancer*. On the *winter solstice* day when $\delta = -23.44°$, the sun shines most directly on the earth's latitude $\varphi_{\text{T-CAP}} = -23.44°$, known as the *Tropic of Capricorn*. The longitude at the Greenwich prime meridian $\lambda_{\text{PM}} = 0°$ [68]. The solar declination angle can be calculated using a geocentric reference frame with the sun located on a *celestial sphere* and earth located at the center of the *celestial sphere*, according to Eq. (8) [60].

$$\delta = arcsin(\sin\lambda_{\text{e}} \cdot \sin\varepsilon) \tag{8}$$

In Eq. (8), λ_{e} represents the *ecliptic longitude* of the sun, that is the sun's angular position along its apparent orbit in the *plane of the ecliptic*. The *plane of the ecliptic* is tilted by the *obliquity of the ecliptic* angle $\varepsilon = 23.44°$ representing the angle between the *plane of the ecliptic* and the plane of the *celestial equator*, the latter being earth's equator projected onto the *celestial sphere*. The ecliptic intersects the equatorial plane at the points corresponding to the *spring*

and fall equinoxes occurring approximately on March 21 and September 21, respectively with $\lambda_e = 0°$ at the March 21 equinox. The Eq. (8) is usually formulated in terms of the day number in a year to account approximately for the elliptic nature of earth's orbit around the sun, as given by Eq. (9) [69].

$$\begin{aligned}\delta =&[0.006918 - 0.399912\cos(\Gamma) + 0.070257\sin(\Gamma) - 0.006758\cos(2\Gamma) + 0.000907\sin(2\Gamma)\\ &- 0.002697\cos(3\Gamma) + 0.00148\sin(3\Gamma)](180/\pi)\end{aligned} \tag{9}$$

In Eq. (9), the solar declination angle δ, is given as a function of the day angle $\Gamma = 2\pi(N_{day} - 1)$ / 365, with day number N_{day}, in a year where $N_{day} = 1$ corresponds to January 1st. The Eq. (9) provides sufficient accuracy due to the relatively small eccentricity value e in Eq. (7). The Eq. (9) shows that the solar illumination of the earth's surface throughout the year occurs most directly between tropical latitudes, namely, the *Tropic of Cancer* ($\delta \approx +23.44°$) and the *Tropic of Capricorn* ($\delta \approx -23.44°$). At the time of the *vernal and autumnal equinoxes*, the earth's equator is located in the *plane of the sun* and every location on earth receives 12 hours of sunlight.

The PV devices can only generate significant electric power during daylight hours therefore, it is essential to verify that a specific geographic location on earth as defined by the latitude φ, and longitude λ, will receive sufficient hours of high incident solar irradiance during the year, before constructing the self-contained sodium (Na) metal production plant. To accurately describe the sun's position in the sky from sunrise to sunset as well as the resulting number of daylight hours, the apparent solar time (AST) is used to express the time of the day. The sun crosses the meridian of the observer at the *local solar noon* when AST = 12, however, the latter time does not coincide exactly with the 12:00 noon time of the locality of the observer. A conversion between the local standard time (LST) and the AST can be made by using equation of time (ET) and longitude corrections. The equation of time accounts for the length of the day variation as a result of the slight eccentricity of the earth's orbit around the sun as well as the tilt of the earth's axis of rotation with respect to a line perpendicular to the plane of its elliptical orbit around the sun. The ET is given by Eq. (10) and has the dimension of minutes [69, 70].

$$\mathrm{ET} = [0.000075 + 0.001868\cos(\Gamma) - 0.032077\sin(\Gamma) - 0.014615\cos(2\Gamma) - 0.04089\sin(2\Gamma)](229.18) \tag{10}$$

The relation between the AST and LST can be made using Eq. (11) that includes the ET and longitude correction which accounts for the fact that the sun traverses 1° of longitude in 4 minutes.

$$\mathrm{AST} = \mathrm{LST} + \mathrm{ET} + (4\ \mathrm{min/deg})(\lambda_S - \lambda_L) - \mathrm{DST} \tag{11}$$

In Eq. (11), the local longitude λ_L, represents the exact longitude value for the location relative to the Greenwich prime meridian of $\lambda_{PM} = 0°$. The standard longitude λ_S, is calculated from λ_L as $\lambda_S = 15° \times (\lambda_L / 15°)$ where the quantity in the parentheses is rounded to an integer value. In Eq. (11), if λ_L is east of λ_S then the longitude correction is positive and if λ_L is west of λ_S then the longitude correction is negative, while DST = 0 minutes or 60 minutes depending on whether daylight savings time applies. If in effect, DST occurs from March until November.

http://dx.doi.org/10.5772/67597

The hour angle h, represents the angular distance in degrees between the longitude λ, of the observer and the longitude whose plane contains the sun, and is calculated according to Eq. (12) [60].

$$h = 15 \cdot (\mathrm{AST} - 12) \tag{12}$$

In Eq. (12), the multiplier of 15° arises because the earth rotates around its own axis 15° in 1 hour, and the AST has a value 0 < AST < 24 hours. When the sun reaches its maximum angle of elevation at the longitude of the observer, it corresponds to the *local solar noon* time where $h = 0°$. The solar elevation angle α_s, above the observer's horizon and its complement, the solar zenith angle θ_{sz}, can be calculated according to Eq. (13) [60].

$$\sin(\alpha_s) = \cos(\theta_{sz}) = \sin(\varphi)\sin(\delta) + \cos(\varphi)\cos(\delta)\cos(h) \tag{13}$$

The solar azimuth angle γ_s, in the horizontal plane of the observer is given by Eq. (14) [60].

$$\cos(\gamma_s) = \frac{\sin(\delta)\cos(\varphi) - \cos(\delta)\sin(\varphi)\cos(h)}{\cos(\alpha_s)} \tag{14}$$

The Eq. (14) uses the convention of the solar azimuth angle defined as positive clockwise from north meaning that east corresponds to 90°, south corresponds to 180° and west corresponds to 270°. The solar azimuth angle provided by Eq. (14) should be interpreted as $0° \le \gamma_s \le 180°$ when $h < 0°$, meaning the sun is located east of the observer, and interpreted as $180° \le \gamma_s \le 360°$ when $h > 0°$, meaning the sun is located west of the observer. The sunrise equation allows to calculate the number of hours of sunlight per day that depends on the solar declination angle δ, and on latitude φ, as shown in Eq. (15), which is derived from Eq. (13) by setting $\alpha_s = 0°$ and solving for h.

$$H_{ss} = -H_{sr} = \frac{1}{15}\arccos[-\tan(\varphi)\tan(\delta)] \tag{15}$$

In Eq. (15), the hour angle h, has a value $-180° < h < 0°$ at sunrise and $0° < h < +180°$ at sunset, and when divided by 15°/hour, yields the number of hours before and after the *local solar noon* time (AST = 12) when $h = 0°$, corresponding to sunrise H_{sr}, and sunset H_{ss}, respectively. Using Eqs. (9) and (15), it is possible to calculate for any geographic location on earth the number of daylight hours on any specific day of the year. The maximum angle of solar elevation $\alpha_{s\text{-}max}$, above the observer's horizon that occurs at the *local solar noon* time is calculated according to Eqs. (16) and (17) that are derived from Eq. (13) by setting $h = 0°$.

$$\alpha_{s-\max} = 90^{\circ} - (\varphi - \delta) \tag{16}$$

$$\alpha_{s-\max} = 90^{\circ} + (\varphi - \delta) \tag{17}$$

The Eq. (16) is applicable for the northern hemisphere while Eq. (17) is applicable for the southern hemisphere. Formulations for the solar declination, elevation, azimuth and zenith angles which account with greater accuracy for the elliptic nature of earth's orbit around the sun exist in the scientific literature often as part of solar position algorithms however, they can be rather complex

[71–76]. The air mass can be calculated as a function of the true solar zenith angle θ_{sz}, given by Eq. (13), considering the effect of atmospheric refraction, according to Eq. (18) [77].

$$\mathrm{AM} = \frac{1.002432\cos^2(\theta_{sz}) + 0.148386\cos(\theta_{sz}) + 0.0096467}{\cos^3(\theta_{sz}) + 0.149864\cos^2(\theta_{sz}) + 0.0102963\cos(\theta_{sz}) + 0.000303978} \tag{18}$$

The direct normal total (spectrally integrated) solar irradiance as a function of the air mass (AM) and atmospheric conditions that include the effects of elevation, can be calculated using the Parameterization Model C developed by Iqbal, given in Eq. (19) [78–80].

$$Irr_n = 0.9751 \cdot E_0 \cdot Irr_0 \cdot \tau_r \tau_o \tau_g \tau_w \tau_a \tag{19}$$

In Eq. (19), $Irr_0 = 1367$ W/m^2, represents the solar constant or total irradiance of the AM 0 standard solar spectral irradiance in space prior to attenuation by earth's atmosphere and the factor 0.9751 is included because the spectral interval of 0.3–3.0 μm is used by the detailed SOLTRAN model from which the Parameterization Model C is derived. The factor E_0, represents the effect of the eccentricity of earth's orbit around the sun on the solar constant Irr_0, due to the periodically varying distance between the earth and sun, as given by Eq. (20) [69].

$$\begin{aligned} E_0 = (r_{\mathrm{sun}-m}/r_{\mathrm{sun}})^2 &= 1.000110 + 0.034221\cos(\Gamma) + 0.001280\sin(\Gamma) \\ &+ 0.000719\cos(2\Gamma) + 0.000077\sin(2\Gamma) \end{aligned} \tag{20}$$

In Eq. (19), the symbol τ_r represents transmittance by Rayleigh scattering, τ_o represents transmittance by ozone, τ_g represents transmittance by uniformly mixed gases, τ_w represents transmittance by water vapor and τ_a represents transmittance by aerosols. The expressions for τ_r, τ_o, τ_g, τ_w, τ_a are given in Eqs. (21–25).

$$\tau_r = \exp[-0.0903 \cdot \mathrm{AM}_a^{0.84}(1.0 + \mathrm{AM}_a - \mathrm{AM}_a^{1.01})] \tag{21}$$

$$\tau_o = 1 - [0.1611 \cdot U_3(1.0 + 139.48 \cdot U_3)^{-0.3035} - 0.002715 \cdot U_3(1.0 + 0.044U_3 + 0.0003U_3^2)^{-1}] \tag{22}$$

$$\tau_g = \exp[-0.0127 \cdot \mathrm{AM}_a^{0.26}] \tag{23}$$

$$\tau_w = 1 - 2.4959 \cdot U_1[(1.0 + 79.034U_1)^{0.6828} + 6.385U_1]^{-1} \tag{24}$$

$$\tau_a = \exp[-k_a^{0.873}(1.0 + k_a - k_a^{0.7088})\mathrm{AM}_a^{0.9108}] \tag{25}$$

In Eqs. (21), (23) and (25), AM_a represents the air mass at the actual atmospheric pressure P and is given as $\mathrm{AM}_a = \mathrm{AM} \times (P / P_0)$ where AM, calculated using Eq. (18), corresponds to standard atmospheric pressure $P_0 = 101325$ Pa. The actual atmospheric pressure P, can be calculated using the isothermal atmosphere formula in Eq. (26).

$$P = P_0 \cdot exp\left[\frac{-g_0 \cdot M_{\mathrm{air}} \cdot h_{\mathrm{PV}}}{R_g T}\right] \tag{26}$$

http://dx.doi.org/10.5772/67597

The Eq. (26) can be used to calculate the atmospheric pressure P in pascals (Pa) at an elevation h_{PV}, in meters (m) above mean sea level, assuming a constant ambient atmospheric temperature T in Kelvin (K), over the difference in elevations. The molar mass of air $M_{air} = 0.028964$ kg/mol, earth's gravitational acceleration near the surface $g_0 = 9.80665$ m/sec^2, and the universal gas constant $R_g = 8.3144621$ J/K·mol [43, 81, 82]. In Eq. (22), $U_3 = l_o \times$ AM, where l_o represents the vertical ozone layer thickness in centimeters (cm) at normal temperature and surface pressure (NTP), and AM is given by Eq. (18). The vertical ozone layer thickness is assumed in the present work to have a mean annual value $l_o = 0.35$ cm (NTP). In Eq. (24), $U_1 = w'(P/101325)^{0.75}\,(273/T)^{0.5} \times$ AM, where w' represents the precipitable water vapor thickness in centimeters (cm) under the actual atmospheric conditions with pressure P in pascals (Pa), and temperature T in Kelvin (K). In Eq. (25), k_a represents the aerosol optical thickness and has a range $0 < k_a < 1$, depending on how clear or aerosol saturated the atmosphere is. The value of k_a is generally measured at the optical wavelengths of 380 nm and 500 nm due to low ozone absorption and calculated using the formula, $k_a = 0.2758 \cdot k_{a|\lambda=380\,nm} + 0.35 \cdot k_{a|\lambda=500\,nm}$. The aerosol optical thickness can vary daily, however, it is assumed in the present work to have a mean annual value $k_a = 0.1$ reflecting clear days.

In **Table 2**, geographic and climate characteristics are specified for four prospective locations of the scalable, self-contained solar powered electrolytic sodium (Na) metal production plant including El Paso, Texas; Alice Springs, Australia; Bangkok, Thailand and Mbandaka, Democratic Republic of Congo (DRC).

	[a]Geographic coordinates φ, λ & elevation h_{PV} (m)	[b]Mean monthly temperature T (°C)	[c]Mean annual precipitable water w' (cm)	Mean annual *local solar noon* air mass (AM)
El Paso	+31.807°, –106.377°/ 1206	17.7	1.27	1.27
Alice Springs	–23.807°, +133.902°/ 545.2	20.5	1.9	1.16
Bangkok	+13.693°, +100.75°/ 1.524	28.2	4.52	1.08
Mbandaka	+0.0225°, +18.288°/ 316.9	25.1	3.81	1.04

[a]Accurate geographic coordinates and elevations above mean sea level for largest commercial airports of respective cities.
[b][83].
[c][84–87].

Table 2. Geographic and climate characteristics for four prospective plant locations.

In **Table 2**, the geographic coordinates use the sign convention of +/– latitude φ, for locations north and south of the equator, respectively, and +/– longitude λ, for locations east and west of the prime meridian ($\lambda_{PM} = 0°$). According to the Köppen-Geiger climate classification system, El Paso has an arid, desert, cold (BWk) climate, Alice Springs has an arid, desert, hot (BWh) climate, Bangkok has a tropical, savanna (Aw) climate and Mbandaka has a tropical, rainforest (Af) climate [88]. The mean annual *local solar noon* air mass values in **Table 2** are calculated using Eqs. (9) and (16)–(18), and the length of day results provided by Eq. (15), show that proximity to the equator for the self-contained sodium (Na) metal production plant maximizes the solar irradiance and provides uniform hours of daylight per day throughout the year. Tropical regions however, experience higher mean monthly temperatures and consequently higher mean annual precipitable water

vapor levels with a long rainy season and sun obscuring rain clouds. Other factors that can significantly affect incident solar irradiance on the PV device panels include the geographic elevation above mean sea level and aerosols comprising solid and liquid sunlight obscuring particulates in the air that can occur naturally due to dust storms and volcanic activity or from human activity such as slash and burn agriculture [89]. According to the accumulated world meteorological data, the southwestern region of the U.S.A. and the central region of Australia, both constitute nearly ideal locations for the self-contained sodium (Na) metal production plants due to the existence of an arid, desert climate, vast tracts of flat open land, sparse human population and many clear days with high solar irradiance throughout the year [47, 48, 90, 91].

3. Sodium metal production plant architecture

The architecture of the self-contained sodium (Na) metal production plant has to provide an optimal balance between high performance, reliability and cost effective operation. The highest performance can be achieved by constructing the solar tower of the plant shown in **Figure 2**, in a manner that allows the optical k-vectors from the sun to be normally incident onto the photovoltaic (PV) device panels throughout the entire period of daylight from sunrise to sunset. The **Figure 4** shows a solar tower architecture with fixed PV device panels, wherein the panels can rotate and tilt with the solar tower as a single unit to follow the sun's overhead trajectory.

In **Figure 4**, the solar tower is fabricated using modular sections comprised of high strength, lightweight aluminum alloy that can be fitted end to end and bolted together until the final slant height of the structure $S_h = 300$ m is achieved. Up to $N_{B\text{-}L/R} = 100$ branches that constitute levels, comprised of modular sections each having a final length $B_l = 50$ m, extend out on each side from the central column of the solar tower resulting in a width for the structure of approximately $S_w = 100$ m. The PV device panels are mounted along the top and bottom of the branches projecting from the central column of the solar tower. The projecting branches of the solar tower also enable ground glass, light diffusing panels to be placed between the rows of solar panels that allow sunlight to penetrate and effectively illuminate the land area beneath the solar tower to support crop cultivation including rice paddy fields. The central column of the solar tower is fixed at the base to a static pylon and approximately midway up the height of the column, to a boom for elevating the solar tower to a tower elevation angle $\pi/2 - \alpha_s$, that is the complement of the solar elevation angle α_s, the latter given in Eq. (13). The opposite end of the boom is fixed to the center of a railroad flatcar mounted on a linear train track that is capable of being displaced along the track to elevate and lower the solar tower. An electric motor module mounted midway up the height of the column enables the PV device panels to collectively rotate left and right about the axis of the central column to track the solar azimuth angle γ_s, the latter given in Eq. (14), thereby allowing the optical k-vectors from the sun to impinge at normal incidence onto the PV device panels throughout most of the day of operation. When the sun has set at the end of the day or when inclement weather of sufficient severity is expected, the solar tower can be lowered to be parallel and nearly flush with the ground as shown in **Figure 4**, with metal louvers drawn over the PV device panels to safeguard against damage to the panels from storms, strong winds and flying debris that can occur, albeit rarely, in the southwestern U.S.A. [92, 93].

http://dx.doi.org/10.5772/67597

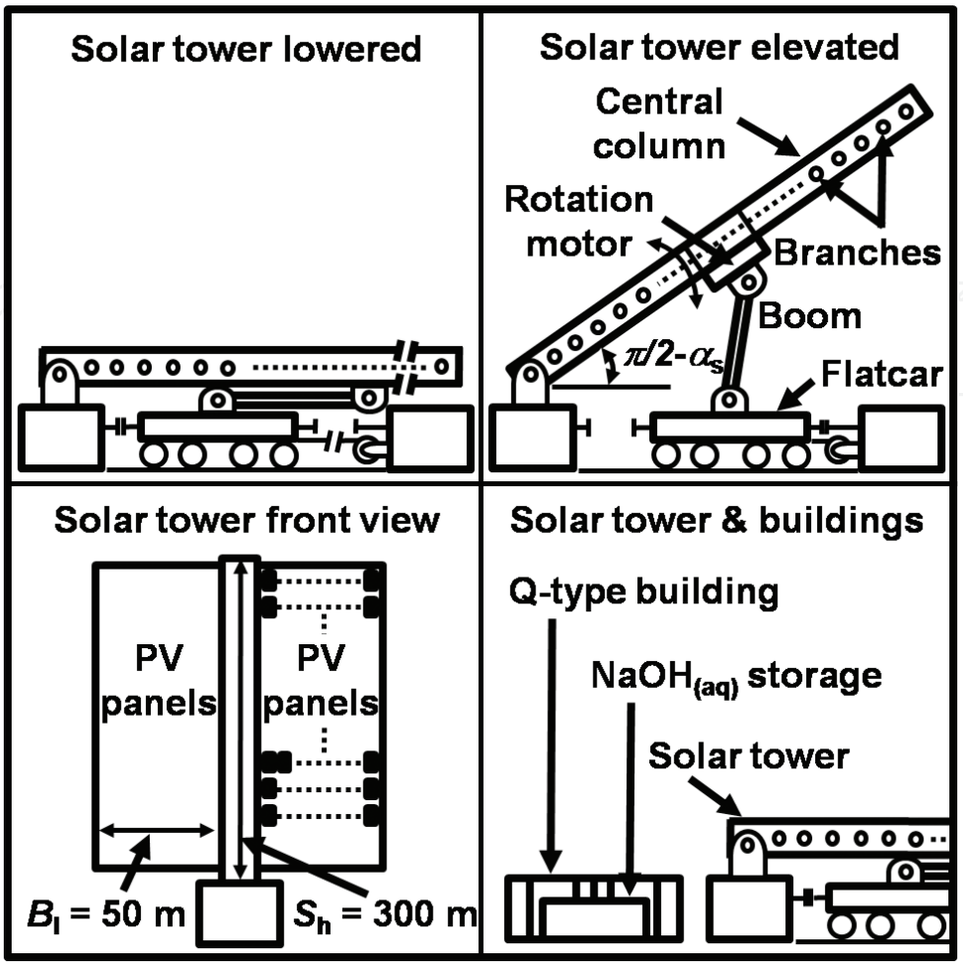

Figure 4. Solar tower architecture (NOT TO SCALE).

3.1. Electrical design of the solar tower

The electrical design of the solar tower comprising PV device panels has to accommodate scalability in the power output level, where it is possible to supplant the existing PV device panels with newer and more efficient ones when they become available, without having to modify other components in the solar tower. It is therefore necessary to optimally dimension the electrical conductors embedded within the branches and central column that transmit the electric power generated by the photovoltaic (PV) device panels to the electrolytic cells, according to the magnitude of the current expected to be transmitted once $\eta_{PV} = 90\%$ efficient PV device panels become available to be installed on the branches of the tower as shown in **Figure 4**. To develop an accurate design for the aluminum current carrying conductors of the solar tower, it becomes necessary to define the electrical interconnection topology of the photovoltaic (PV) device panels installed on the solar tower. In **Figure 5**, the equivalent circuit model of the photovoltaic (PV) device panel array installed on the solar tower is shown, with the corresponding straight line approximation of the current versus voltage curve for the PV device panel array.

In the circuit models shown in **Figure 5**, I_{PV} represents the PV device current, V_{OC} represents the PV device open circuit voltage, R_P represents the parallel resistance of the PV device that ideally

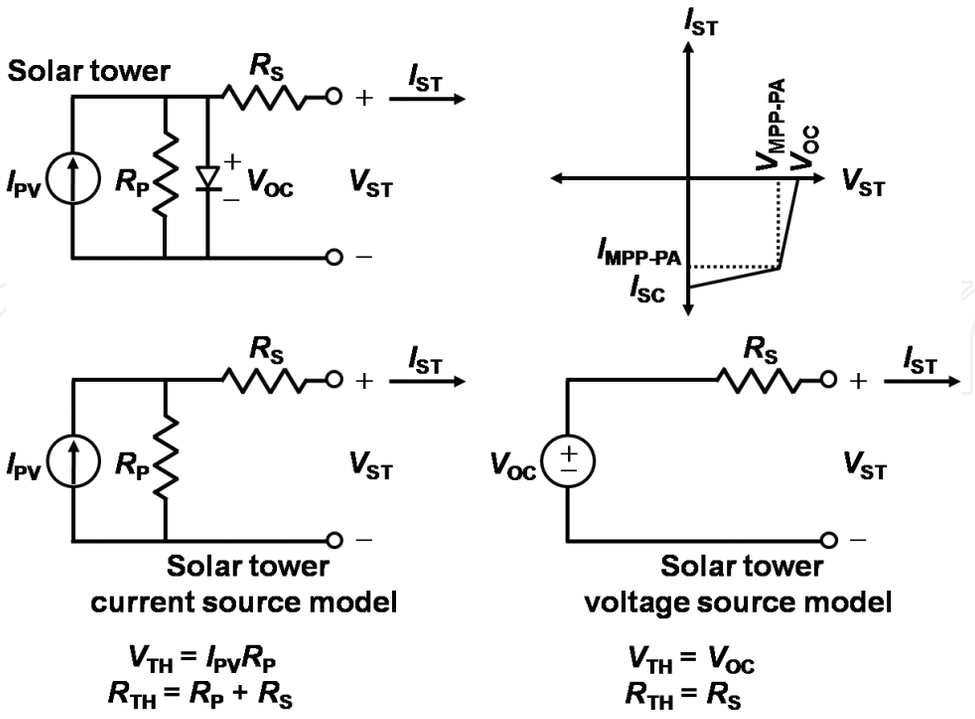

Figure 5. Circuit model of the photovoltaic (PV) device panel array installed on the solar tower.

should be infinite, R_S represents the series resistance of the PV device that ideally should be zero in value, I_{ST} represents the output current of the solar tower and V_{ST} represents the output voltage of the solar tower. The circuit models shown in **Figure 5** are applicable for a single PV cell as well as for an array of PV device panels comprised of PV cells connected in series and/or in parallel [94]. The expressions for the Thevenin equivalent circuit voltage V_{TH} and resistance R_{TH}, are given both for the linear equivalent current source and voltage source circuits. The electrical interconnection topology of the PV device panels on the solar tower must achieve an optimal balance in operating parameters including the solar tower supply system maximum voltage $V_{ST\text{-}MAX}$ and maximum current $I_{ST\text{-}MAX}$. It will be assumed in the further analysis and calculations that $V_{ST\text{-}MAX}$ corresponds to the maximum power point (MPP) operating voltage of the PV device panel array ($V_{MPP\text{-}PA}$) rather than to the open circuit voltage V_{OC}, of the array and similarly, that $I_{ST\text{-}MAX}$ corresponds to the MPP operating current of the PV device panel array ($I_{MPP\text{-}PA}$) rather than to the short circuit current I_{SC}, of the array. The assumptions can be considered valid since it is possible to show using Eqs. (27)–(29) that there exists only a small difference in the value between $V_{MPP\text{-}PA}$ and V_{OC} and similarly between $I_{MPP\text{-}PA}$ and I_{SC} if R_P is large and R_S is small. The Eqs. (27)–(29) describe the solar tower PV array model shown in **Figure 5**.

$$I_{PV} = I_{SC}\frac{(R_S + R_P)}{R_P} \tag{27}$$

$$\frac{V_{MPP-PA}}{I_{SC} - I_{MPP-PA}} = R_S + R_P \tag{28}$$

$$\frac{V_{OC} - V_{MPP-PA}}{I_{MPP-PA}} = R_S \tag{29}$$

http://dx.doi.org/10.5772/67597

The Eq. (27), can be derived from the circuit model in **Figure 5** by short circuiting the output terminals of the solar tower where $I_{ST} = I_{SC}$. The Eq. (28) is calculated from the solar tower PV array operating as a current source at the maximum power point (MPP), and Eq. (29) is calculated from the solar tower PV array operating as a voltage source at the MPP.

The solar tower must be capable of transmitting $P_{ST} = 23.9$ MW of electric power as indicated in **Figure 3**, from the photovoltaic (PV) device panels to the electrolytic cells of the scalable, sodium (Na) metal production plant while maintaining reasonable design values for $V_{ST\text{-}MAX}$ and $I_{ST\text{-}MAX}$ that will not escalate the cost of the system. To achieve an optimal balance between the $V_{ST\text{-}MAX}$ and $I_{ST\text{-}MAX}$ parameters of the solar tower supply system, it is necessary to identify the most reliable and cost effective approach for maintaining the PV devices at or near their maximum power point (MPP) during operation. Many methods exist for providing a variable or dynamic load to PV devices and performing maximum power point tracking (MPPT), however, for the present application it is necessary to consider that since there are up to $N_P = 30{,}000$ PV device panels installed on the solar tower, it becomes uneconomical to use any approach that requires dedicated MPPT hardware for so many panels individually or even for small groups of panels and therefore, a collective solution is required for the entire PV device panel array having an area $A_{PA} = 30{,}000$ m^2. A reliable method of operating PV devices very near, if not exactly at the MPP can be implemented by controlling the output voltage of the PV devices [95]. The maximum power point output voltage of a single PV cell $V_{MPP\text{-}C}$, is always very near in value to a temperature dependent operating voltage of the PV cell and this phenomenon can be used to implement a type of MPPT by controlling the output voltage V_{ST}, of the entire PV device panel array with area $A_{PA} = 30{,}000$ m^2. The output voltage V_{ST} of the entire PV device panel array can be controlled for example, by using a voltage step down pulse width modulated (PWM) DC-DC converter with closed loop feedback control that is operated at the proper duty cycle required to maintain the input voltage V_{IN}, to the converter (which is equivalent to the output voltage V_{ST}, of the PV device panel array), at the value near to the MPP voltage. In practice, the MPP output voltage of a single junction, monocrystalline silicon PV cell is given as $V_{MPP\text{-}C} \approx 0.4$ V which is too low for direct input to a PWM DC-DC converter [95]. Commercial single junction, front-illuminated, monocrystalline silicon PV panels of the type shown in **Table 1**, typically contain 60 PV cell modules connected in series resulting in a maximum power point output voltage for the panel given as $V_{MPP\text{-}P} = 30.1$ V for the NU-U240F2 Sharp panel, $V_{MPP\text{-}P} = 31.9$ V for the LG280S1C-B3 LG panel and $V_{MPP\text{-}P} = 31.7$ V for the STP290S-20 Suntech panel. The maximum power point output voltage of the 96 module, back-illuminated SPR-X21-345 Sunpower panel is given as $V_{MPP\text{-}P} = 57.3$ V. The series connected PV cell modules use bypass diodes to prevent power loss from an entire chain of series connected cells if one cell becomes shaded, and receives less illumination than other cells causing its resistance to increase, by allowing energy to be collected from PV cells that are not shaded and are outside of the bypassed section of the chain containing the shaded cell(s) [96, 97]. If 15 of the standard 60 cell module single junction, front-illuminated, monocrystalline silicon PV panel types are connected together in series, then the solar tower supply system maximum voltage can be limited to approximately $V_{ST\text{-}MAX} \approx 450$ VDC, which corresponds to a *low voltage* supply according to the International Electrotechnical Commission (IEC) that defines *low voltage* DC equipment as having a nominal voltage below 750 VDC [98]. A *low*

voltage DC supply system entails a minor risk of electric arcing through the air and an exemption from specialized protection equipment needed for *high voltage*. If 15 of the 96 cell module, back-illuminated SPR-X21-345 Sunpower PV panels are connected together in series, then the solar tower supply system maximum voltage $V_{\text{ST-MAX}} \approx 900$ VDC, which exceeds by 150 V the nominal 750 VDC IEC standard of a *low voltage* supply. Once $\eta_{\text{PV}} = 90\%$ efficient PV device panels will become available, it is expected that they will each have an area $A_{\text{P}} = 1$ m^2 and the number of PV cell modules connected together in series will yield a maximum power point voltage for the panel given as $V_{\text{MPP-P}} \approx 30$ V that is similar in value to most of the commercial single junction, front-illuminated, monocrystalline silicon PV panels listed in **Table 1**, that contain 60 PV cell modules connected in series. Under an ASTM AM 1.5G standard terrestrial solar spectral irradiance with a total irradiance $Irr_{\text{AM1.5G}} = 1000$ W/m^2, the corresponding maximum power point current of the $\eta_{\text{PV}} = 90\%$ efficient PV panel can be calculated as $I_{\text{MPP-P}} = (\eta_{\text{PV}} \times Irr_{\text{AM1.5G}}) / V_{\text{MPP-P}} = 30.0$ A, which is a substantially larger current than the $I_{\text{MPP-P}}$ current values listed in **Table 1**, as might be expected for the more efficient PV panel unit. Therefore, it is necessary to design the current conductors within the scalable solar tower to be capable of transmitting the substantially larger current of more efficient PV panels once they will become available for installation onto the solar tower. The solar tower supply system maximum voltage can be set to $V_{\text{ST-MAX}} = 450$ V, achieved by connecting in series 15 PV device panels with an efficiency $\eta_{\text{PV}} = 90\%$ and $V_{\text{MPP-P}} \approx 30$ V, mounted on a single branch section of the solar tower apparatus as shown in **Figure 6**.

In **Figure 6**, each branch section supports the installation of 2 groups of 15 series connected PV panels having an efficiency $\eta_{\text{PV}} = 90\%$ for a total $N_{\text{P-Bsec}} = 30$ PV panels per branch section. A total of 5 branch sections should be fastened together end to end, to yield $N_{\text{P-B}} = 5 \times N_{\text{P-Bsec}} = 150$ PV panels per branch with 5 groups of 15 series connected PV panels installed along the top of the branch and another 5 groups of 15 series connected PV panels installed along the bottom of the branch. Each branch section has a length $Bsec_{\text{l}} = 10$ m, and contains embedded within the aluminum current conductors, yielding a branch length $B_{\text{l}} = 50$ m as shown in **Figure 4**. The groups of 15 series connected PV panels are electrically connected to a pair of aluminum conductors inside the branch, resulting in parallel electrical interconnection for the groups of 15 series connected PV panels that increases the electric current delivered by the solar tower. Each PV panel has a width $P_{\text{w}} = 0.66$ m and a height $P_{\text{l}} = 1.5$ m for a total PV panel area given as $A_{\text{P}} = P_{\text{w}} \times P_{\text{l}} = 1$ m^2. Since the height of each PV panel is given as $P_{\text{l}} = 1.5$ m, then each branch has an overall height given as $B_{\text{h}} = 2 \times P_{\text{l}} = 3$ m. The solar tower that has a height $S_{\text{h}} = 300$ m as shown in **Figure 4**, can therefore accommodate up to 100 branches extending out from the left and right sides of the central column, yielding a total PV panel array area on the solar tower given as $A_{\text{PA}} = 2 \times (S_{\text{h}} / B_{\text{h}}) \times N_{\text{P-B}} \times A_{\text{P}} = 30{,}000$ m^2.

The electric current from each branch section flows into the electrical conductors installed inside the central column of the solar tower as shown in **Figure 6**. Therefore, electric current that flows from the outermost branch section toward the central column increases as each branch section contributes additional current generated by the 30 PV panels mounted on it. If an ASTM direct normal AM 1.5D standard terrestrial solar spectral irradiance with a total irradiance $Irr_{\text{AM1.5D}} = 887$ W/m^2, is incident on the PV panels having an efficiency $\eta_{\text{PV}} = 90\%$ and $V_{\text{MPP-P}} = 30$ V, then the maximum power point output current can be calculated as $I_{\text{MPP-P}} = (\eta_{\text{PV}} \times Irr_{\text{AM1.5D}}) /$

http://dx.doi.org/10.5772/67597

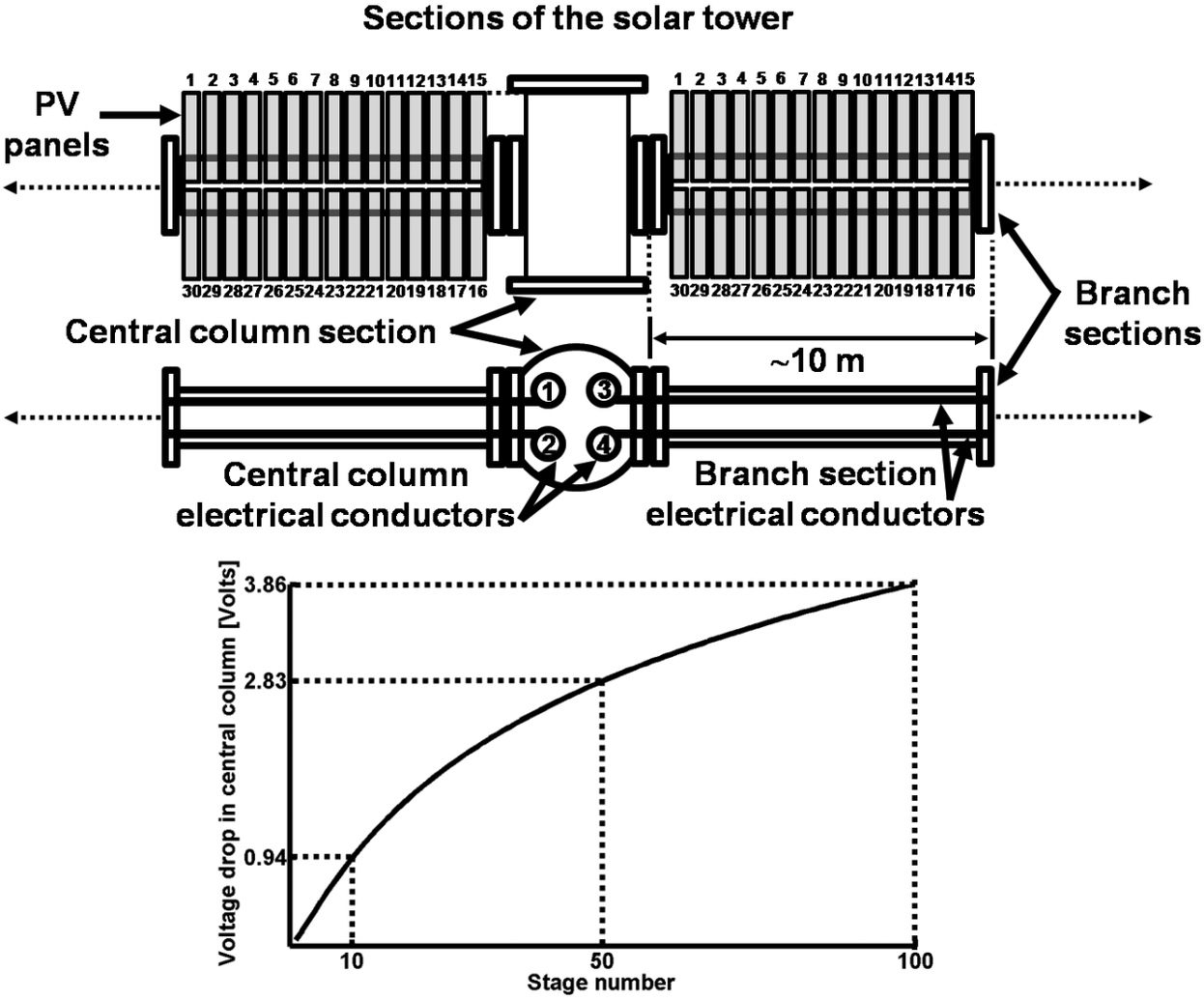

Figure 6. Solar tower branch sections showing groups of 15 series interconnected PV device panels installed.

($V_{MPP\text{-}P}$) = 26.6 A. The result for $I_{MPP\text{-}P}$ = 26.6 A, entails that each branch section will contribute $I_{Bsec} = 2 \times I_{MPP\text{-}P} = 53.2$ A. Therefore, the current in each branch increases by $I_{Bsec} = 53.2$ A as it flows in from the outermost branch section toward the current conductors of the central column of the solar tower. The total current contributed by each branch of the solar tower is then calculated as $I_B = 5 \times I_{Bsec} = 266$ A, since a single branch comprises 5 branch sections. Each side of the solar tower has $N_{B\text{-}L/R} = 100$ branches for a total number of branches on the solar tower given as $N_{B\text{-}ST} = 2 \times N_{B\text{-}L/R} = 200$ branches. It is convenient however, to install four electrical conductors labeled 1, 2, 3 and 4, in the central column of the solar tower as shown in **Figure 6**. The first pair of current conductors 1 and 2, transmits current from the branches mounted on the left side of the solar tower and the second pair of current conductors 3 and 4, transmits current from the branches mounted on the right side of the solar tower, so that each conductor pair only needs to transmit a maximum current $I_{ST\text{-}MAX} = 26{,}600$ A.

The four electrical conductors installed within the modular sections of the central column of the solar tower that are located at or near the top of the solar tower, do not have to carry the maximum current $I_{ST\text{-}MAX} = 26{,}600$ A, rather only the four electrical conductors installed in the

bottom most modular section of the central column have to be dimensioned to transmit the maximum current. The diameters of aluminum electrical conductors within the central column sections scale linearly from a diameter $D_{S1} = 2$ cm in stage 1 at the top to $D_{S100} = 41.6$ cm for stage 100 at the bottom of the solar tower, the latter that transmits the maximum current $I_{ST\text{-}MAX} = 26{,}600$ A. **Figure 6**, shows the calculated voltage drop across the aluminum electrical conductors in all 100 modular sections of the central column of the solar tower to be given as $V_{ST\text{-}DROP} = 3.86$ V, corresponding to a low loss considering that the solar tower supply system maximum voltage $V_{ST\text{-}MAX} = 450$ V.

The electrical design of the solar tower described provides manifold advantages including a mostly parallel electrical interconnection architecture for the PV device panels that allows the MPP of the PV device panels to be controlled collectively by controlling the output voltage V_{ST} of the PV device panel array using a voltage step down PWM DC-DC converter designed to have a constant output voltage V_{OUT}, and controllable input voltage V_{IN}, the latter supplied from the PV device panel array and equal to V_{ST}, shown in **Figure 5**. Other advantages include a *low voltage* DC solar tower supply system with optimal balance between the maximum voltage $V_{ST\text{-}MAX} \approx 450$ V and maximum current $I_{ST\text{-}MAX} = 26{,}600$ A, wherein two independent and electrically isolated power supply feeds are provided from the left side branches and right side branches of the solar tower apparatus, respectively. Yet another important advantage of the design includes a low center of gravity for the solar tower apparatus due to the modular sections comprising the central column being heavier near the base and lighter near the top as a result of larger diameter aluminum electrical conductors placed near the base of the tower.

3.2. Electrical design of the sodium hydroxide electrolysis plant

The solar tower apparatus described in Section 3.1 implements a mostly parallel electrical interconnection architecture for the PV device panels that yields two identical, independent and electrically isolated low voltage DC power supplies, each having a maximum voltage $V_{ST\text{-}MAX} \approx 450$ V and maximum current $I_{ST\text{-}MAX} = 26{,}600$ A, wherein the two power supply feeds emanate from the left side branches and right side branches of the solar tower apparatus, respectively as shown in **Figure 6**. The sodium hydroxide (NaOH) electrolysis cell however, requires a substantially lower voltage for operation. The quantity of sodium (Na) metal produced by the NaOH electrolytic cell depends fundamentally on the magnitude of the DC current flowing between the anode and cathode terminals of the electrolysis cell. The Eqs. (4)–(6) provide the standard reduction potentials of the oxidation and reduction half reactions that occur at the anode and cathode, respectively of the electrolytic cell. In practice, the electrolytic cell operating voltage has to be set at approximately $V_{CELL} = 4$ V for electrolysis of pure NaOH or $V_{CELL} = 5$ V for electrolysis of a mixture of NaOH and NaCl, the latter derived from sea salt. The higher voltage accounts for the overvoltage effects [99]. The maximum current that can be supplied to an electrolytic cell operating at approximately $V_{CELL} \approx 5$ V will be $I_{CELL} \approx 100{,}000$ A and is limited in large measure by the material cost as well as by the mass and physical dimensions of the electrical conductors required to transmit such magnitude of the current.

In a fused or molten state, $NaOH_{(l)}$ is highly corrosive and therefore the only conventional materials capable of withstanding prolonged exposure to its caustic effects at an elevated

http://dx.doi.org/10.5772/67597

temperature include graphite, iron and nickel. Graphite however, cannot be used as an anode electrode because it will react with the oxygen (O_2) generated to produce carbon dioxide (CO_2) and become consumed in the process. Iron can withstand corrosion from fused $NaOH_{(l)}$, and consequently could be used to fabricate the electrolytic vessel however, as an anode electrode, the reaction with steam ($H_2O_{(g)}$) and O_2 will quickly oxidize and erode iron. The only material suitable for fabricating both the anode and cathode electrodes remains nickel (Ni) which is significantly more expensive than both graphite and iron. The cost of the Ni electrodes therefore becomes an important factor in limiting the maximum current in the electrolytic cell. The other factor limiting the current in the electrolytic cell becomes the PWM DC-DC converter that must supply the large currents at the correct output voltage to the electrolytic cell, safely and reliably.

It is necessary to provide two identical voltage step down PWM DC-DC converters to convert the power $P_{ST\text{-}L/R} = 11.95$ MW delivered by the two independent low voltage DC power supplies of the solar tower, each having a maximum voltage $V_{ST\text{-}MAX} \approx 450$ V and maximum current $I_{ST\text{-}MAX} = 26{,}600$ A. The PWM DC-DC converter must be designed to safely convert the electric power supplied from the solar tower to magnitudes of DC voltage and DC current that are appropriate for supplying the NaOH electrolytic cells. The PWM DC-DC converters and electrolytic cells are housed together inside the prefabricated Q-type metal building indicated in **Figure 4**. If each PWM DC-DC converter is designed to supply a single NaOH electrolytic cell with a power conversion efficiency $\eta_{DC\text{-}DC} = 100\%$, then the maximum current in the single NaOH electrolytic cell would be calculated as $I_{OUT} = (V_{ST\text{-}MAX} \times I_{ST\text{-}MAX}) / V_{CELL} = (450\text{ V}) \times (26{,}600\text{ A}) / 5\text{ V} = 2{,}394{,}000$ A, a value that is clearly beyond the practical realm. Consequently, multiple NaOH electrolytic cells have to be constructed and electrically connected in series to be supplied by a cell current $I_{CELL} = 96{,}500$ A that corresponds to approximately one mole of electrons supplied per second [43]. The output voltage of the PWM DC-DC converter is then calculated as $V_{OUT} = (V_{ST\text{-}MAX} \times I_{ST\text{-}MAX}) / I_{CELL} = (450\text{ V}) \times (26{,}600\text{ A}) / 96{,}500\text{ A} = 124$ V. The number of NaOH electrolytic cells that must be connected in series to be supplied by a single PWM DC-DC converter is calculated as $V_{OUT} / V_{CELL} = 124\text{ V} / 5\text{ V} \approx 25$ cells. Therefore, the self-contained sodium (Na) metal production plant has a total of 50 NaOH electrolytic cells with 2 sets of 25 cells electrically connected in series and supplied by two identical PWM DC-DC converters that function as voltage step down converters to transform the output voltage of the solar tower V_{ST}, which represents a DC input voltage to the converter unit $V_{IN} = V_{ST\text{-}MAX} \approx 450$ V, to a constant DC output voltage $V_{OUT} = 124$ V with high efficiency, while controlling the PWM DC-DC converter input voltage V_{IN}, and thereby output voltage V_{ST} of the solar tower PV device panels to maintain their operation near the MPP.

The design of voltage step down PWM DC-DC converters that have a fixed output voltage V_{OUT} and control the input voltage V_{IN} that is variable, has been an active topic of research in the context of photovoltaic power systems applications [94, 95]. The requirements of the present application however, entail a specialized type of large scale direct photovoltaic power conversion for chemical electrolysis not hitherto contemplated or addressed in the scientific/industrial literature. The design for the voltage step down PWM DC-DC converter with a fixed output voltage V_{OUT} and variable input voltage V_{IN} meant to supply the NaOH electrolytic

cells is shown in **Figure 7** to consist of a multiphase converter topology, with synchronous voltage step down converter circuits connected in parallel.

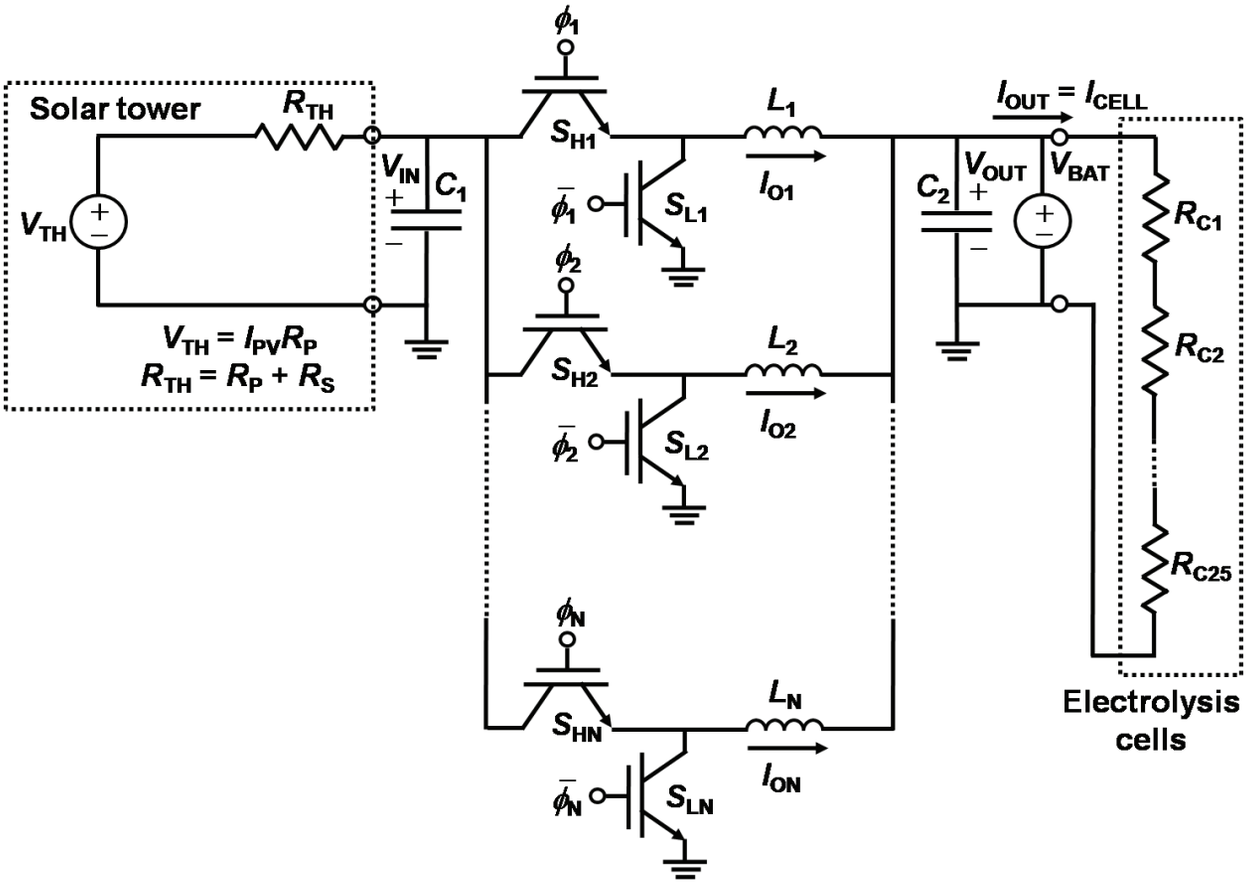

Figure 7. Multiphase voltage step down PWM DC-DC converter power supply for NaOH electrolytic cells.

The synchronous parallel multiphase voltage step down PWM DC-DC converter power supply shown in **Figure 7** offers the inherent advantage of allowing the large load current $I_{OUT} = I_{CELL} = 96{,}500$ A to be split among the phases of the converter to match the current carrying capacity of the individual electronic switches, that in practice would consist of power insulated gate bipolar transistors (IGBTs) such as the Model 1MBI3600U4D-120, manufactured by the Fuji Electric Company with a maximum rated collector-emitter voltage and collector-emitter current given as $V_{CE} = 1{,}200$ V (at $T_C = 25$ °C) and $I_{CE} = 3{,}600$ A (at $T_C = 80$ °C), respectively. It is possible to use 64 such IGBT devices in up to $N_\phi = 32$ phases of the multiphase PWM DC-DC converter with 2 IGBT devices per phase as shown in **Figure 7**, to deliver the required current $I_{OUT} = I_{CELL} = 96{,}500$ A to the 25 series connected NaOH electrolytic cells indicated as having resistances R_{C1}, R_{C2}, …, R_{C25}, without exceeding the electrical ratings of the solid state switches. Using a multiphase converter topology with synchronous voltage step down converter circuits connected in parallel, also allows the current $I_{CELL} = 96{,}500$ A to be split among the 32 inductors L_1–L_{32}, present in each of the $N_\phi = 32$ phases, thereby not requiring one single large inductor to transmit the full current I_{OUT}, supplied by the PWM DC-DC converter to the

http://dx.doi.org/10.5772/67597

load comprising the electrolytic cells. Current sharing occurs between the synchronous voltage step down converter circuits connected in parallel according to Eq. (30).

$$I_{O1} + I_{O2} + \ldots + I_{ON} = I_{OUT} \tag{30}$$

Assuming the ideal case that current sharing between synchronous parallel voltage step down converter circuits is equal, then $I_{O1} = I_{O2} = \ldots = I_{ON} = I_{OUT} / N_{\phi}$ where $I_{ON} = I_{OUT} / N_{\phi} =$ (96,500 A / 32) = 3,016 A transmitted per phase. Thus, each of the 32 inductors L_1–L_{32}, can be designed for a current load $I_{ON} = 3{,}016$ A, a value well within the capabilities of inductor manufacturers. The output voltage of the multiphase voltage step down PWM DC-DC converter can be set to a fixed value using a utility scale battery, and thus $V_{BAT} = V_{OUT} = 124$ V. The input voltage V_{IN}, of the multiphase voltage step down PWM DC-DC converter power supply for electrolytic cells shown in **Figure 7**, that also corresponds to the output voltage V_{ST}, of the solar tower PV device array has to be controlled reliably to ensure that the PV device panel array operates at or near its maximum power point (MPP).

The synchronous parallel multiphase voltage step down PWM DC-DC converter power supply in **Figure 7** with $N_{\phi} = 32$ phases, constitutes a complicated nonlinear dynamical system that can be challenging to model, control and analyze accurately to ensure stable operation under wide ranging conditions [100]. The closed loop control system using voltage control and a single feedback loop that can be applied to the present converter is shown in **Figure 8**.

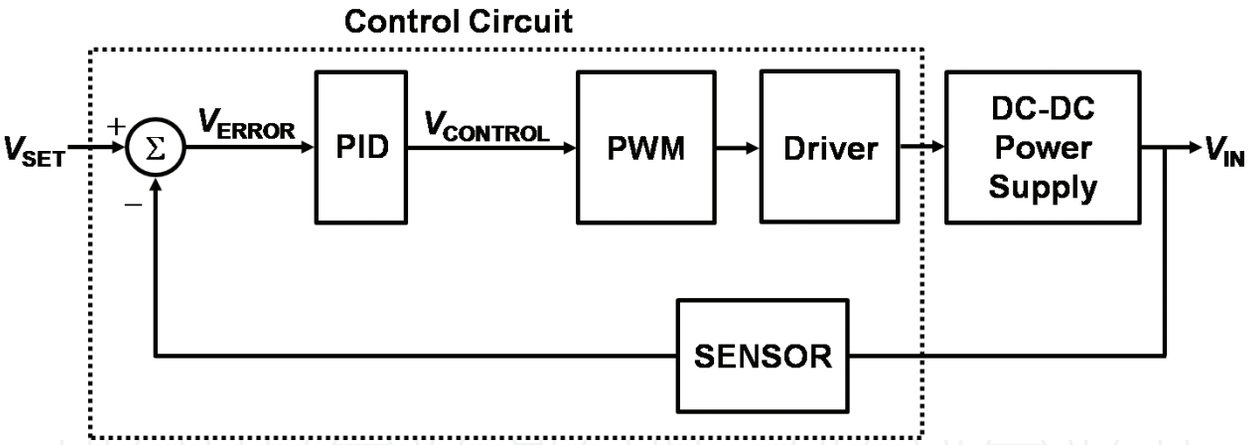

Figure 8. Closed loop control system for the multiphase voltage step down PWM DC-DC converter.

The control system for the multiphase voltage step down PWM DC-DC converter shown in **Figure 8** consists of a sensor that senses the process parameter to be controlled, namely, the input voltage V_{IN} to the PWM DC-DC converter that is also the output voltage V_{ST}, of the solar tower PV device panel array. The error amplifier compares the scaled process parameter V_{IN} to the set point value V_{SET} and computes the difference as an error signal V_{ERROR}. A proportional, integrator, differentiator (PID) circuit processes the error signal V_{ERROR}, and accordingly generates a control signal $V_{CONTROL}$, that is supplied to a pulse width modulation (PWM) signal generation circuit to produce the control signals that have the correct frequency, duty cycle and phase shift. The PWM signal to the IGBT switches has to be replicated $N_{\phi} = 32$ times and phase

shifted by $\phi_{\text{Shift}} = 360^\circ / N_\phi = 11.25^\circ$ using a driver circuit to control all the synchronous voltage step down converters connected in parallel in **Figure 7**. In **Figure 9**, the electronic circuit schematics for some of the different control blocks in **Figure 8** are shown.

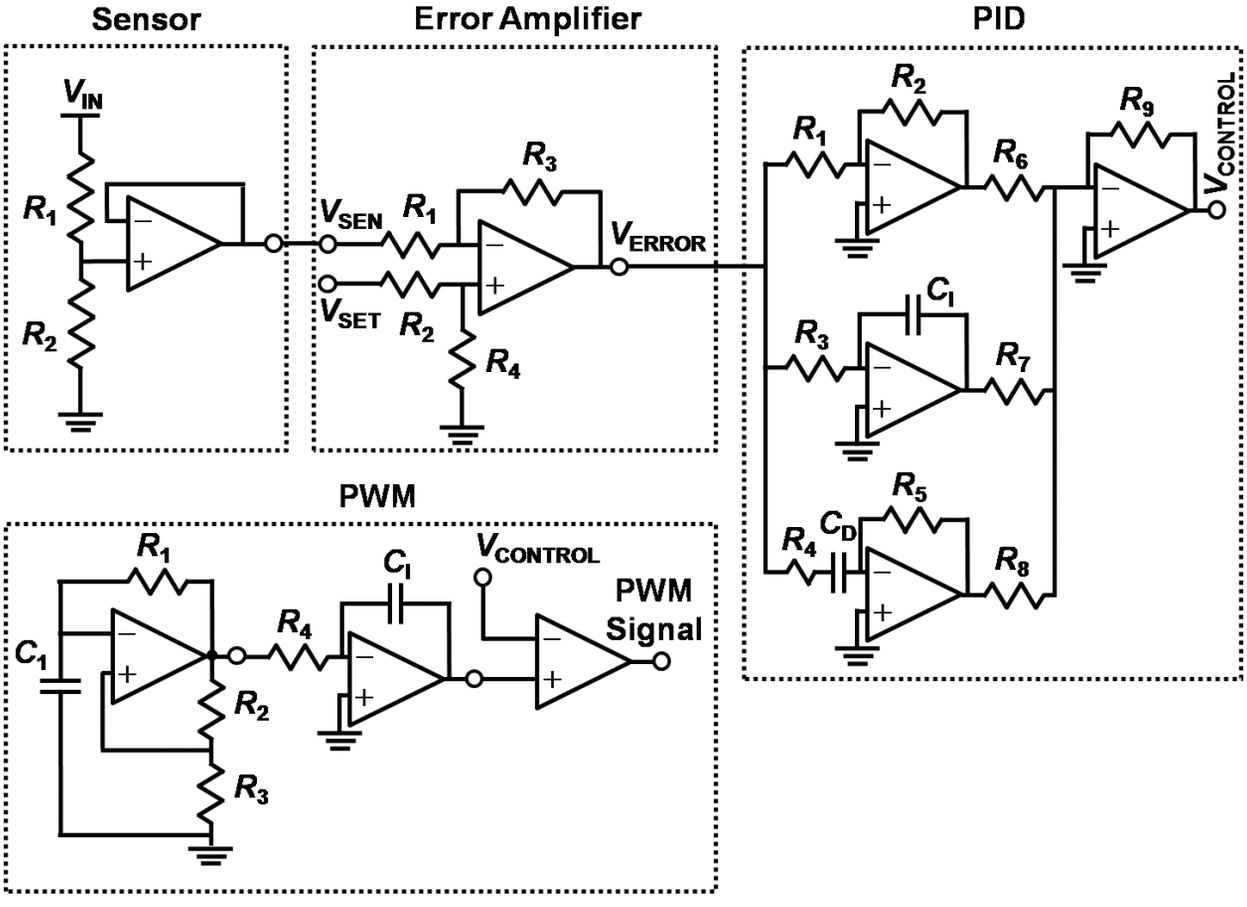

Figure 9. Electronic circuit schematics of the control system for the multiphase voltage step down PWM DC-DC converter.

The electronic circuits shown in **Figure 9** are representative of the functional blocks of the PWM DC-DC converter control system. The sensor circuit can consist of a resistive voltage divider with a unity gain op-amp buffer that senses the voltage V_{IN}, at the input of the PWM DC-DC converter according to Eq. (31).

$$V_{\text{SEN}} = V_{\text{IN}} \times (R2 / R1 + R2) \tag{31}$$

The error amplifier subtracts the input voltage V_{SEN}, scaled by the resistive voltage divider of the sensor circuit, from the set point reference voltage V_{SET}, to calculate an error voltage V_{ERROR}, according to Eq. (32).

$$V_{\text{ERROR}} = (R3 / R1) \times (V_{\text{SET}} - V_{\text{SEN}}) \text{ where } R1 = R2 \text{ and } R3 = R4 \tag{32}$$

The PID unit receives the error voltage V_{ERROR}, as an input and produces a control voltage V_{CONTROL}, given as Eq. (33).

http://dx.doi.org/10.5772/67597

$$V_{\mathrm{CONTROL}}(t) = G_{\mathrm{P}}\left(V_{\mathrm{ERROR}}(t)\right) + G_{\mathrm{I}}\int_0^t V_{\mathrm{ERROR}}(t)dt + G_{\mathrm{D}}\frac{dV_{\mathrm{ERROR}}(t)}{dt} \tag{33}$$

In Eq. (33), the terms G_{P}, G_{I} and G_{D} represent the gains of the proportional, integrator and differentiator circuits, respectively that can be tuned as needed to achieve optimal control characteristics for the PWM DC-DC converter. There exist myriad other ways of controlling the PWM DC-DC converter using only proportional (P) and integrator (I) control functions without the differentiator (D) circuit for example, however, the control system shown in **Figures 8** and **9**, represents a robust and reliable type of control of the PWM DC-DC converter. The PWM unit is shown to consist of a fixed frequency square wave voltage oscillator with an op-amp integrator circuit that converts the square wave into a triangular wave ramp signal which is then compared to the control voltage V_{CONTROL}, from the PID circuit using a comparator, to generate the PWM signal for the IGBT electronic switches of the PWM DC-DC converter. The driver circuit that generates the $N_{\phi} = 32$ copies of the PWM signal from **Figure 8**, with each signal and its complement phase shifted by $\phi_{\mathrm{Shift}} = 11.25^{\circ}$ for all 64 IGBT switches in the converter is not shown in **Figure 9**. It could be implemented however, using all digital logic. The control system allows the PWM DC-DC converter to be effectively controlled by setting just one parameter, namely, the reference voltage V_{SET}, to a value that corresponds with the maximum power point (MPP) output of the solar tower PV device panel array to transmit the maximum power available from the PV devices to the NaOH electrolytic cells.

It is possible to gain insight into the operation of the synchronous parallel multiphase voltage step down PWM DC-DC converter with attached solar tower PV device panel array, from the most common modeling approach using small signal analysis based on state space averaging [101]. The open loop transfer function $G_{\mathrm{V}}(\mathrm{s})$, of the voltage step down PWM DC-DC converter that yields the small signal response of the input voltage process parameter $V_{\mathrm{IN}} = V_{\mathrm{ST}}$ to the duty cycle control variable d, can be calculated straightforwardly by making the simplifying assumption, namely, that the power supply has a single phase ($N_{\phi} = 1$) rather than $N_{\phi} = 32$ phases in parallel as depicted in **Figure 7**. The voltage step down PWM DC-DC converter from **Figure 7** with only a single phase ϕ_1, can be characterized by two pairs of differential equations that describe the current I_{O1}, flowing through the inductor L_1, and the voltage V_{IN}, across the input capacitor C_1, during the two distinct states of the converter when the switch S_{H1} is closed and open. The pair of differential equations corresponding to the switch S_{H1} being closed are given by Eqs. (34) and (35).

$$L_1\frac{dI_{\mathrm{O1}}}{dt} = V_{\mathrm{IN}} - V_{\mathrm{OUT}} \tag{34}$$

$$C_1\frac{dV_{\mathrm{IN}}}{dt} = \frac{V_{\mathrm{TH}} - V_{\mathrm{IN}}}{R_{\mathrm{TH}}} - I_{\mathrm{O1}} \tag{35}$$

The pair of differential equations corresponding to the switch S_{H1} being open are given by Eqs. (36) and (37).

$$L_1 \frac{dI_{O1}}{dt} = -V_{OUT} \tag{36}$$

$$C_1 \frac{dV_{IN}}{dt} = \frac{V_{TH} - V_{IN}}{R_{TH}} \tag{37}$$

The state space form of the above four differential equations describing the PWM DC-DC converter having just a single phase ϕ_1, is given as Eqs. (38) and (39) for S_{H1} being closed and open, respectively.

$$\frac{d}{dt}\begin{bmatrix} I_{O1} \\ V_{IN} \end{bmatrix} = \begin{bmatrix} 0 & \frac{1}{L_1} \\ -\frac{1}{C_1} & -\frac{1}{C_1 R_{TH}} \end{bmatrix}\begin{bmatrix} I_{O1} \\ V_{IN} \end{bmatrix} + \begin{bmatrix} -\frac{1}{L_1} & 0 \\ 0 & \frac{1}{C_1 R_{TH}} \end{bmatrix}\begin{bmatrix} V_{OUT} \\ V_{TH} \end{bmatrix} \tag{38}$$

$$\frac{d}{dt}\begin{bmatrix} I_{O1} \\ V_{IN} \end{bmatrix} = \begin{bmatrix} 0 & 0 \\ 0 & -\frac{1}{C_1 R_{TH}} \end{bmatrix}\begin{bmatrix} I_{O1} \\ V_{IN} \end{bmatrix} + \begin{bmatrix} -\frac{1}{L_1} & 0 \\ 0 & \frac{1}{C_1 R_{TH}} \end{bmatrix}\begin{bmatrix} V_{OUT} \\ V_{TH} \end{bmatrix} \tag{39}$$

The Eq. (38), has the form $\dot{x} = A_1 x + B_1 u$, and Eq. (39) has the form $\dot{x} = A_2 x + B_2 u$. The averaged state space equation can be expressed in a similar form $\dot{x} = Ax + Bu$, where the A and B matrices are calculated based on the duty cycle d, of the switch S_{H1}, the matrices A_1, B_1, A_2, B_2 and are given as $A = d \cdot A_1 + (1 - d) \cdot A_2$ and $B = d \cdot B_1 + (1 - d) \cdot B_2$. The vector x, in the averaged state space equation contains the average values of the state variables $<I_{O1}>$ and $<V_{IN}>$ and the vector u, contains the input variables V_{OUT} and V_{TH} that are considered as DC values.

When all transients in the PWM DC-DC converter have stabilized and steady state operation is achieved, then $\dot{x} = 0$, thus the averaged state space equation can be used to express the DC steady state equations given as Eqs. (40) and (41).

$$\dot{x} = 0 = AX + BU \tag{40}$$

$$X = \begin{bmatrix} I_{O1} \\ V_{IN} \end{bmatrix} = -A^{-1}BU = -\frac{L_1 C_1}{D^2}\begin{bmatrix} -\frac{1}{C_1 R_{TH}} & -\frac{D}{L_1} \\ \frac{D}{C_1} & 0 \end{bmatrix}\begin{bmatrix} -\frac{1}{L_1} & 0 \\ 0 & \frac{1}{C_1 R_{TH}} \end{bmatrix}\begin{bmatrix} V_{OUT} \\ V_{TH} \end{bmatrix} \tag{41}$$

Calculating out Eq. (41) yields the DC value results given in Eqs. (42) and (43) for I_{O1} and V_{IN}.

$$I_{O1} = \frac{V_{TH}}{R_{TH} D} - \frac{V_{OUT}}{R_{TH} D^2} \tag{42}$$

$$V_{IN} = \frac{V_{OUT}}{D} \tag{43}$$

The result in Eq. (43) allows to calculate the DC value duty cycle D, needed to maintain the input voltage V_{IN}, of the PWM DC-DC converter that is equal to the output voltage of the solar tower $V_{ST} = V_{IN} = 450$ V. Thus, the duty cycle $D = V_{OUT} / V_{IN} = 124$ V / 450 V = 0.28.

http://dx.doi.org/10.5772/67597

The linear model of the open loop transfer function $G_V(s)$, for the voltage step down PWM DC-DC converter at the operating point that can be used to evaluate small signal variations in the duty cycle control variable d used to control the voltage V_{IN}, can be developed by adding a small signal AC perturbation to the DC value D, of the duty cycle. Since a positive increase of the duty cycle d, causes a decrease in V_{IN} as confirmed by Eq. (43), it becomes convenient for modeling purposes to express the duty cycle in terms of a new variable $d' = 1 - d = D' + \hat{d}'$, where D' is the DC value of d' and $\hat{d}'$ is the small signal AC perturbation. The linear model of the open loop transfer function for the PWM DC-DC converter provides the response to the small signal AC perturbations $\hat{d}'$ around the DC value D'. The averaged state space equation can be formulated in terms of the new variable d' according to Eq. (44).

$$\dot{x} = \Big((1-d')A_1 + (d')A_2\Big)x + \Big((1-d')B_1 + (d')B_2\Big)u \tag{44}$$

In Eq. (44), the vector $x = X + \hat{x}$ and vector $u = U + \hat{u}$, where each vector comprises the DC value and a small signal perturbation. The Eq. (44) can be expanded as shown in Eq. (45).

$$\begin{aligned}\frac{d(X+\hat{x})}{dt} &= \Big((1-D^{'}-\hat{d}')A_1 + (D^{'}+\hat{d}')A_2\Big)(X+\hat{x}) + \Big((1-D^{'}-\hat{d}')B_1 + (D^{'}+\hat{d}')B_2\Big)(U+\hat{u}) \\ &= XA_1 + XD^{'}(-A_1+A_2) + X\hat{d}^{'}(-A_1+A_2) + \hat{x}A_1 + \hat{x}D^{'}(-A_1+A_2) + \hat{x}\hat{d}^{'}(-A_1+A_2) \\ &\quad + UB_1 + UD^{'}(-B_1+B_2) + U\hat{d}'(-B_1+B_2) + \hat{u}B_1 + \hat{u}D^{'}(-B_1+B_2) + \hat{u}\hat{d}'(-B_1+B_2)\end{aligned} \tag{45}$$

In Eq. (45), discarding the DC and nonlinear terms yields Eq. (46).

$$\begin{aligned}\frac{d\hat{x}}{dt} &= \hat{x}A_1 + \hat{x}D^{'}(-A_1+A_2) + \hat{d}^{'}\Big((-A_1+A_2)X + (-B_1+B_2)U\Big) \\ &= \hat{x}A + \hat{d}'\Big((-A_1+A_2)X + (-B_1+B_2)U\Big)\end{aligned} \tag{46}$$

Taking the Laplace transform of the averaged state space equation which has the form $\dot{x} = Ax + Bu$, yields the result in Eq. (47).

$$sX(s) - x(0) = AX(s) + BU(s) \tag{47}$$

In Eq. (47), $x(0)$ represents the initial value of the state vector in the time domain. For calculating the transfer function it is assumed that $x(0) = 0$. Solving Eq. (47) for $X(s)$ yields the result in Eq. (48).

$$X(s) = (sI_n - A)^{-1}x(0) + (sI_n - A)^{-1}BU(s) \tag{48}$$

Applying the Laplace transform to Eq. (46), yields the result given in Eq. (49).

$$s\hat{x}(s) = \hat{x}(s)A + \hat{d}'(s)\Big((-A_1+A_2)X + (-B_1+B_2)U\Big) \tag{49}$$

Solving Eq. (49) for $\hat{x}(s)$ yields the result in Eq. (50).

$$\hat{x}(s) = (s\begin{bmatrix}1 & 0\\ 0 & 1\end{bmatrix} - A)^{-1}\hat{d}'(s)\Big((-A_1 + A_2)X + (-B_1 + B_2)U\Big) \tag{50}$$

The open loop transfer function given as $G_V(s) = \hat{x}(s)/\hat{d}'(s)$ of the PWM DC-DC converter can be obtained by calculating out Eq. (50) to yield the result in Eq. (51).

$$G_{\mathrm{V}}(s) = \frac{R_{\mathrm{TH}}(V_{\mathrm{IN}}D + sL_1I_{\mathrm{O1}})}{s^2L_1C_1R_{\mathrm{TH}} + sL_1 + D^2R_{\mathrm{TH}}} \tag{51}$$

The analysis to yield the open loop transfer function for the multiphase voltage step down PWM DC-DC converter with $N_\phi = 32$ phases requires creating a map that contains all the state space equations describing all possible states of the 64 IGBT switches during a period of duration T_{P}, corresponding to a cycle of operation of the PWM DC-DC converter. For $N_\phi = 32$ phases, there will be in effect 32 switching events occurring per cycle of operation with a phase shift $\phi_{\mathrm{Shift}} = 11.25°$. Thus, there will exist 32 state space equations of the form given in Eq. (52).

$$\dot{x} = A_ix + B_iu \tag{52}$$

In Eq. (52), the matrices A_i and B_i describe the PWM DC-DC converter in the subinterval of duration t_i between switchings of the parallel phases where $\sum_{i=1}^{N_\phi} t_i = T_{\mathrm{P}}$. The solutions from Eq. (52) can be stacked to yield a discrete time equation valid over an entire period T_{P} that effectively represents a map for the multiphase PWM DC-DC converter [100]. The state space averaging method used to obtain the open loop transfer function of the PWM DC-DC converter with a single phase given in Eq. (51), can also be applied to calculate the open loop transfer function for the PWM DC-DC converter with $N_\phi = 32$ phases in parallel shown in **Figure 7** [101]. An analysis of the present $N_\phi = 32$ phase, closed loop multiphase PWM DC-DC converter including stability analysis, is highly complex especially when considering parametric variations among the parallel voltage step down converter circuits, and will be described in future work. It is also possible, to operate the multiphase PWM DC-DC converter in an open loop control mode, where a plant operator monitors and controls the electrical resistance of the electrolytic cells, and manually adjusts the duty cycle of the PWM DC-DC converter to deliver maximum power to the electrolytic cells. The plant operator balances the currents I_{O1}–I_{O32}, flowing in each phase of the PWM DC-DC converter by manually adjusting the amplitudes of the PWM control signals supplied to the gate terminals of the IGBT switches.

4. Sodium metal production plant operating characteristics

The solar cycle described in Section 2.2, the electrical design of the solar tower described in Section 3.1, and the electrical design of the sodium hydroxide (NaOH) electrolysis plant described in Section 3.2, entail that the voltage step down pulse width modulated (PWM) DC-DC converter supplying electricity from the solar tower PV device panel array directly to the NaOH electrolytic cells has to be operated according to a precise protocol.

http://dx.doi.org/10.5772/67597

Prior to sunrise occurring, the sodium hydroxide (NaOH) electrolytic cells are replenished to capacity with concentrated aqueous $NaOH_{(aq)}$ solution from the storage tanks shown in **Figure 2**, that are located adjacent to the Q-type metal building that houses electrical switch gear, voltage step down (PWM) DC-DC power converter units, the sodium hydroxide (NaOH) electrolytic cells, sodium (Na) metal packaging unit and chlorine (Cl_2) gas separation and bottling unit. As sunrise commences, the solar tower photovoltaic (PV) device panel array begins generating electric power. The voltage step down PWM DC-DC converter supplies the electric power from the solar tower PV device panel array to the electrolytic cells at a fixed voltage given as $V_{BAT} = V_{OUT} = 124$ V. Before NaOH electrolysis and Na metal production can begin, the liquid aqueous $NaOH_{(aq)}$ has to be heated to evaporate all of the water ($H_2O_{(l)}$) content and fuse or melt the remaining anhydrous solid $NaOH_{(s)}$. The presence of water or moisture in the NaOH being electrolyzed can significantly reduce Na metal yield due to side reactions occurring between the Na metal and residual H_2O. The sodium hydroxide melts into a liquid state at $T_f = 594 \pm 2$ K [102]. Therefore, electric power delivered by the solar tower initially at sunrise, has to be transmitted to electric heating elements for evaporating the water ($H_2O_{(l)}$) from the aqueous $NaOH_{(aq)}$ and to raise the temperature of the fused anhydrous $NaOH_{(l)}$ to the proper temperature for electrolysis. Once the proper temperature of the fused anhydrous $NaOH_{(l)}$ is reached, current from the solar tower can be transmitted to the cathode and anode electrodes of the 25 electrolytic cells electrically connected in series, to begin production of Na metal according to Eqs. (2) and (3).

The electric current is supplied to the 25 electrolytic cells electrically connected in series, by the synchronous parallel multiphase voltage step down PWM DC-DC converter at a fixed output voltage set by the utility scale battery given as $V_{BAT} = V_{OUT} = 124$ V. The current $I_{OUT} = I_{CELL}$, supplied by the PWM DC-DC converter from the solar tower to the electrolytic cells is not constant throughout the day, increasing gradually from sunrise until the sun reaches its zenith, and subsequently decreasing gradually as the sun tracks west and eventually sets. To use the electric power generated by the solar tower PV device panel array most efficiently for Na metal production, it is necessary to configure the electrolytic cells as a variable electric load, wherein their electrical resistance can decrease gradually as the sun arcs toward zenith allowing I_{CELL} to increase as more electric power is generated by the solar tower for electrolysis and subsequently, the electrical resistance of the electrolytic cells can begin to increase gradually as the sun passes beyond the zenith toward sunset, when I_{CELL} must decrease as less electric power is generated by the solar tower for electrolysis.

The sodium (Na) metal production plant can effectively be controlled using only two adjustable parameters, including the set point reference voltage V_{SET}, that controls the input voltage V_{IN}, of the PWM DC-DC converter that is equal to the output voltage of the solar tower $V_{IN} = V_{ST}$, and the electrical resistance of the NaOH electrolytic cells. The set point reference voltage V_{SET} can function either as a coarse or fine adjustment for the current supplied by the solar tower PV device panel array to the electrolytic cells at the fixed voltage $V_{BAT} = V_{OUT} = 124$ V. The electrical resistance of the electrolytic cells naturally increases slowly over time as the fused $NaOH_{(l)}$ reactant is decomposed by the current flowing between the electrodes of the cell according to Eqs. (2) and (3). The electrolytic cells can be designed for example, with a controllable electrical resistance that can remain relatively constant (or increase or decrease as needed) even as the fused $NaOH_{(l)}$ reactant is consumed, by varying the spacing between the

anode and cathode electrodes, where the electrodes can be moved closer together to compensate the loss of reactant volume as it is consumed in the cell.

It is possible to calculate the quantity of Na metal produced throughout the year by the self-contained sodium (Na) metal production plant sited in the different geographic locations given in **Table 2**, based on the hours of daylight and the prevailing air mass conditions. It is not necessary to specify a detailed design for the NaOH electrolytic cell to generate an accurate daily estimate of Na metal production yield throughout the year, if it is assumed that maximum electric power available from the solar tower PV device panel array can always be supplied to the electrolytic cells by appropriately controlling the electrical resistance of the NaOH electrolytic cells together with the set point reference voltage V_{SET} of the PWM DC-DC converter. It is assumed that electrolysis of NaOH, and thereby Na metal production can only occur if the available current supplied by the solar tower PV device panel array has a minimum threshold value of $I_{ST} = 3{,}000$ A. In **Figure 10**, the production yield of Na metal is calculated for each day of the hypothetical year 2015, for electrolysis of pure NaOH according to Eq. (2), for the four geographic locations listed in **Table 2**, using the solar position algorithm (SPA) described in *Solar position algorithm for solar radiation applications* written by Reda & Andreas in 2004, that is a refined algorithm based on the book, *The Astronomical Algorithms* written by Meeus in 1998, and is presently regarded as the most accurate [73, 74]. The SPA allows the solar zenith θ_{sz}, and azimuth γ_s, angles to be calculated with uncertainties of $\pm 0.0003^{\circ}$ in the range between -2000 to 6000 years.

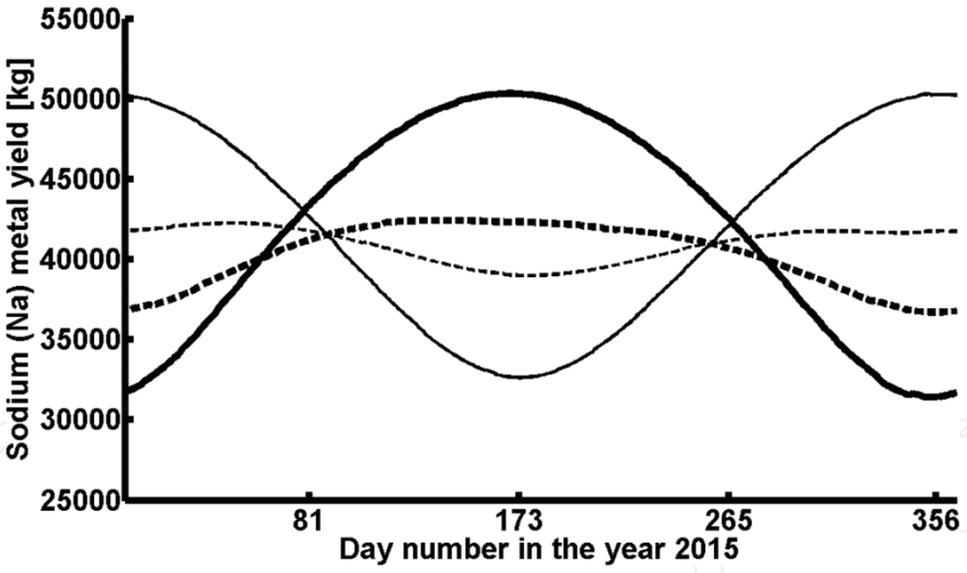

Figure 10. Calculated sodium (Na) metal daily production yields throughout the hypothetical year 2015, for El Paso, Texas (thick solid), Alice Springs, Australia (thin solid), Bangkok, Thailand (thick dash) and Mbandaka, DRC (thin dash).

The calculation in **Figure 10** provides the expected daily sodium (Na) metal production yield under the assumption that the energy conversion efficiency $\eta_{PV} = 90\%$ for the solar tower PV device panel array and furthermore, current is only transmitted to the electrolytic cells when the solar tower PV device panel array receives sufficient solar irradiance to produce the minimum threshold value of current $I_{ST} = 3{,}000$ A. The calculation in **Figure 10**, uses the SPA algorithm to determine the solar zenith angle θ_{sz}, throughout the day from sunrise to sunset for each day of

http://dx.doi.org/10.5772/67597

the hypothetical year 2015, and calculates the air mass (AM) using Eq. (18). The direct normal total (spectrally integrated) solar irradiance incident onto the solar tower PV device panel array is calculated in turn, using Eq. (19) in a real time manner, as the solar position and air mass change throughout the day for each day of the year. The results from **Figure 10**, show that consistent quantities of Na metal are produced throughout the year when the self-contained sodium (Na) metal production plant is located as near as possible to the equator where the length of the day is the most uniform. Further away from the equator, the variability in the length of the day increases however, even at a latitude $\varphi = +31.8^{\circ}$, in El Paso, Texas, the variability in the length of the day is not so significant as to render Na metal production uneconomical during the winter months when the daylight interval becomes reduced. The mean daily sodium (Na) metal production yields for the hypothetical year 2015 are calculated as 41,998 kg/day for El Paso, 41,884 kg/day for Alice Springs, 40,281 kg/day for Bangkok and 40,947 kg/day for Mbandaka, assuming a mean annual aerosol optical thickness value $k_a = 0.1$ reflecting clear days and uninterrupted Na production for all 365 days of the year. Notwithstanding the variability in daily Na metal production throughout the year, El Paso, Texas has the highest elevation above mean sea level when compared with Alice Springs, Bangkok and Mbandaka as shown in **Table 2**, resulting in an increased solar irradiance incident onto the PV device panel array and thus, the highest mean daily Na metal production. A conservative estimate for the true mean daily sodium (Na) metal production yield for the year might be $m_{Na} = 30{,}000$ kg/day of Na metal, as a consequence of nonproductive days due to inclement weather and required plant maintenance. The results in **Figure 10**, clearly demonstrate that the scalable, self-contained solar powered electrolytic sodium (Na) metal production plant can be constructed almost anywhere on earth and especially in the southwestern region of the U.S.A., to achieve a hydrogen ($H_{2(g)}$) fuel, sustainable, closed clean energy cycle.

5. Logistics of sodium hydroxide and sodium metal

For the full benefits of the hydrogen ($H_{2(g)}$) fuel based sustainable clean energy economy to be realized, it is essential to overcome the logistical problems inherent with $H_{2(g)}$ fuel. The $H_{2(g)}$ fuel possesses the unique characteristic that it can be combusted directly inside an internal combustion engine (ICE) to produce useful work without emission of carbon dioxide (CO_2) or sulfur oxides (SO_X) and with minimal emission of nitrogen oxides (NO_X). It can also be converted to electricity directly in a fuel cell to produce useful work with substantially higher efficiency than in an ICE. Regardless of how the versatile $H_{2(g)}$ fuel is applied to produce useful work, it is essential to provide safe, reliable and economical logistics for its use. The major drawback of $H_{2(g)}$ fuel remains the difficulty of direct storage. Fortunately, the element sodium (Na) positioned two rows below hydrogen in Group I of the periodic table of elements, is sufficiently electropositive to be capable of chemically releasing the $H_{2(g)}$ fuel stored in either ordinary salinated (sea) or desalinated (fresh) water (H_2O) over a wide temperature range [37]. Sodium (Na) is also sufficiently abundant in nature in the form of sodium chloride (NaCl) in seawater, to make its use economical for $H_{2(g)}$ fuel generation [103]. Therefore, sodium (Na) metal and the sodium hydroxide (NaOH) byproduct resulting from the $H_{2(g)}$ fuel producing chemical reaction in Eq. (1), constitute the ideal intermediate materials needed to render $H_{2(g)}$ into a practical and usable fuel by storing the sun's radiated energy as Na metal.

A hydrogen ($H_{2(g)}$) fuel clean energy economy based on a sustainable, closed clean energy cycle that uses sodium (Na) metal recovered by electrolysis from sodium hydroxide (NaOH) as a means of storing the sun's radiant energy collected during daytime hours, provides numerous benefits including safe, reliable and economical logistics. The scalable, self-contained sodium (Na) metal production plant that stores the sun's radiant energy in sodium (Na) metal, can be constructed in almost any geographic location on earth benefitting from ample solar irradiance and clear weather all year. In the U.S.A., the arid, southwestern desert region offers the requisite conditions, including sufficient undeveloped land area to construct scalable, self-contained solar powered electrolytic sodium (Na) metal production plants by the thousands. Using the southwestern desert region that includes West Texas, New Mexico, Arizona and Southern California as a hub for solar powered sodium (Na) metal production by electrolysis of sodium hydroxide (NaOH), it is possible to develop sufficient Na metal production capacity based on the scalable, self-contained sodium (Na) metal production plant described, to meet the U.S.A.'s energy needs for motor vehicle transport and for broader clean electric power applications.

The physical and chemical properties of sodium (Na) metal and sodium hydroxide (NaOH) render these materials ideal from an operational logistical standpoint. The sodium (Na) metal is a solid at room temperature and therefore has negligible vapor pressure. As a result, Na metal can be stored almost indefinitely in hermetically sealed packaging that can be opened much as a sardine can, only when the Na metal must be loaded into a hydrogen generation apparatus to react with either salinated (sea) or desalinated (fresh) water (H_2O) according to Eq. (1), to produce hydrogen ($H_{2(g)}$) fuel on demand [37]. The sodium hydroxide (NaOH) byproduct of the hydrogen producing chemical reaction in Eq. (1), is also a solid at room temperature in its pure form and has negligible vapor pressure. The NaOH is miscible with water in all proportions, enabling the aqueous $NaOH_{(aq)}$ solution to be readily transferred by pumping into and out of sealed tanks for transport by truck, rail car or pipeline to the remotely located self-contained sodium (Na) metal production plant units for reprocessing by electrolysis according to Eqs. (2) and (3), to recover the Na metal for reuse in generating $H_{2(g)}$ fuel. The $NaOH_{(aq)}$ transportation/storage tanks of the type shown in **Figure 2**, can be fiberglass or metal with a corrosion resistant internal rubber liner, and must seal hermetically to exclude ambient air that contains carbon dioxide (CO_2) which slowly degrades the $NaOH_{(aq)}$, albeit not irreversibly.

To obtain a sense for the magnitude of the logistical effort needed to produce and distribute sufficient sodium (Na) metal to fuel all of the motor vehicles in the U.S.A. while recovering the sodium hydroxide (NaOH) byproduct for reprocessing by electrolysis, it is necessary to consider the total number of vehicles in circulation. According to the Bureau of Transportation Statistics at the United States Department of Transportation (DOT), the total number of registered vehicles in the year 2013 in the U.S.A. numbered 255,876,822 [104]. The figure includes passenger cars, motorcycles, light duty vehicles, other 2-axle/4-tire vehicles, trucks with 2-axles/6-tires or more and buses. If it is further assumed that each motor vehicle on average consumes the energy equivalent of 16.2 gallons of 100 octane gasoline (2,2,4-Trimethylpentane) per week, then the corresponding quantity of $H_{2(g)}$ fuel having an equivalent heating value is given as 15.8 kg. The generation of 15.8 kg of $H_{2(g)}$ fuel according to

http://dx.doi.org/10.5772/67597

Eq. (1), requires that 361.6 kg of Na metal react with approximately 300 kg of water (H_2O) [37]. Therefore, the total quantity of Na metal consumed per week in the U.S.A. can be calculated as 255,876,822 vehicles × 361.6 kg/week = 92,525,058,835 kg/week. If each solar tower produces a mass m_{Na} = 30,000 kg/day of Na metal, then in one week the Na metal yield per solar tower will be given as 30,000 kg × 7 days = 210,000 kg/week. The number of solar towers required to meet demand for Na metal will be given as N_{ST} = 92,525,058,835 kg/week / 210,000 kg/week = 440,596 solar towers or approximately $N_{ST} \approx$ 450,000 solar towers. While the number of solar towers required might seem very large and the task of constructing them onerous, it is in fact possible to construct the sufficient number of towers to provide Na metal for all the motor vehicles in the U.S.A. The self-contained sodium (Na) metal production plants can be constructed at a density of approximately ρ_{plant} = 30 plant units per square mile to prevent mutual shading when the towers are elevated and rotated to track the sun. The solar tower density and layout necessitate a land area given as $A_{land} = N_{ST} / \rho_{plant}$ = 450,000 / 30 = 15,000 square miles, to meet the Na metal demand for all the motor vehicles in the U.S.A. using PV device panels with an efficiency η_{PV} = 90%, and a land area A_{land} = 75,000 square miles using PV device panels with an efficiency η_{PV} = 18% that currently exist commercially. The land area required can be placed into perspective when considering that the area of the state of New Mexico is approximately 121,000 square miles and thus, there exists more than sufficient desert land area for constructing the scalable, self-contained sodium (Na) metal production plants in the U.S.A.

Our company believes that hydrogen ($H_{2(g)}$) fuel will earn an important role in motor vehicle transport applications for powering smaller 1–5 kW class secondary power fuel cells for onboard continuous recharging of battery electric vehicles (BEVs), a concept implemented successfully in the 1960s using $H_{2(g)}$ fuel stored in high pressure cylinders [23]. The concept of a smaller hydrogen fuel cell operating at a fixed power output level to continuously recharge an electric storage battery can be extended not only to motor vehicle propulsion systems but also for a broad range of clean electric power applications, including general ground transport that includes commercial trucks, trains, maritime transport as well as powering single family homes, commercial establishments and industrial enterprises. Such an approach will ultimately enable mankind to dispense with use of carbon based fossil fuels for motor vehicle transport applications and most other types of ground based electric power generation.

6. Conclusion

The technical and economic viability of a novel, scalable, self-contained solar powered electrolytic sodium (Na) metal production plant has been demonstrated for meeting the hydrogen ($H_{2(g)}$) fuel clean energy needs of the U.S.A. The scalable, self-contained sodium (Na) metal production plant uses a solar tower PV device panel array to collect and convert the sun's vast radiant energy emission produced by hydrogen fusion, into electric power that is used to recover sodium (Na) metal from sodium hydroxide (NaOH) or from a mixture of NaOH and NaCl by electrolysis. The Na metal can subsequently be reused to

generate $H_{2(g)}$ fuel and NaOH byproduct by reacting with either ordinary salinated (sea) or desalinated (fresh) water (H_2O). The scalable, self-contained sodium (Na) metal production plant operation is enabled by a specially designed voltage step down PWM DC-DC converter consisting of a multiphase converter topology with up to 32 synchronous voltage step down converter circuits connected in parallel. The PWM DC-DC converter has a fixed output voltage $V_{OUT} \approx 124$ V and variable input voltage $V_{IN} = V_{ST}$, that corresponds to the output voltage of the solar tower PV device panel array and can be controlled to maintain the PV device panel array operating near the maximum power point (MPP). Each scalable, self-contained sodium (Na) metal production plant consists of two voltage step down PWM DC-DC converters, wherein each unit supplies 25 NaOH electrolytic cells, electrically connected in series, with a current $I_{CELL} = 96{,}500$ A, corresponding to approximately one mole of electrons per second. The scalable electrical design of the solar tower allows the PV device panel array to be upgraded with newer and more efficient PV device panels as they become available as a result of progress in scientific research and development. Once PV device panels with an efficiency $\eta_{PV} = 90\%$ will become available, the power output of the solar tower PV device panel array can reach $P_{ST} = 23.9$ MW that is sufficient for producing a mass quantity of approximately $m_{Na} = 30{,}000$ kg of Na metal per day from the electrolysis of NaOH. It therefore becomes possible to meet the hydrogen ($H_{2(g)}$) fuel clean energy needs of all the motor vehicles in the U.S.A. by constructing approximately 450,000 scalable, self-contained sodium (Na) metal production plant units of the type described, in the southwestern desert region of the U.S.A. that includes West Texas, New Mexico, Arizona and Southern California. If the land area needed for the scalable, self-contained sodium (Na) metal production plant units becomes scarce, then purpose built ships equipped with the Na metal production plants can be dispatched into the vast ocean expanses near the equator where high solar irradiance occurs, to convert aqueous $NaOH_{(aq)}$ stored onboard into sodium (Na) metal before returning to port.

Nomenclature

a	Length of the semi-major axis of earth's elliptical orbit around the sun	(m)
A, B	Matrices	
A_P	Photovoltaic (PV) panel area	(m^2)
A_{PA}	Photovoltaic (PV) panel array area	(m^2)
A_{land}	Land area	(mi^2)
AM	Air mass at mean sea level	
AM_a	Air mass at actual atmospheric pressure	
B_l	Solar tower branch length	(m)
$Bsec_l$	Solar tower branch section length	(m)
B_h	Solar tower branch height	(m)
d	DC-DC converter duty cycle	

http://dx.doi.org/10.5772/67597

d'	DC-DC converter duty cycle, $d' = 1 - d$	
$\hat{d}'$	DC-DC converter duty cycle small signal AC perturbation	
C	Capacitor value	(F)
D	DC-DC converter duty cycle DC value	
D'	DC-DC converter duty cycle DC value, $D' = 1 - D$	
D_S	Electrical conductor diameter	(cm)
i	Indices	
E_r°, E_o°	Standard reduction, oxidation half reaction potential	(V)
E_{ov}°	Standard overall reaction potential	(V)
E_0	Eccentricity correction for the solar constant	
G_P	Proportional circuit gain	
G_I	Integrator circuit gain	
G_D	Differentiator circuit gain	
G_V	DC-DC converter open loop voltage transfer function	
h	Hour angle	(°)
h_{PV}	Photovoltaic (PV) array elevation above mean sea level	(m)
H_{sr}	Hours between sunrise and *local solar noon*	(hours)
H_{ss}	Hours between *local solar noon* and sunset	(hours)
Irr_n	Direct normal solar irradiance	(W/m^2)
$Irr_{AM1.5D}$	ASTM direct normal AM 1.5D standard terrestrial total solar irradiance	(W/m^2)
$Irr_{AM1.5G}$	ASTM global AM 1.5G standard terrestrial total solar irradiance	(W/m^2)
I_B	Solar tower branch current	(A)
I_{Bsec}	Solar tower branch section current	(A)
I_{ST}	Solar tower output current	(A)
$I_{ST\text{-}MAX}$	Solar tower maximum output current	(A)
I_O	DC-DC converter per phase output current	(A)
I_{OUT}	DC-DC converter output current	(A)
I_{CELL}	Electrolytic cell current	(A)
I_{PV}	Photovoltaic (PV) device current	(A)
I_{SC}	Photovoltaic (PV) panel short circuit current	(A)
$I_{MPP\text{-}P}$	Photovoltaic (PV) panel maximum power point current	(A)
$I_{MPP\text{-}PA}$	Photovoltaic (PV) panel array maximum power point current	(A)
I_{CE}	IGBT collector-emitter current	(A)
k_a	Aerosol optical depth or thickness	
l_o	Vertical ozone layer depth or thickness	(cm (NTP))
L	Inductor value	(H)
m_{Na}	Sodium mass	(kg)

N_P	Number of photovoltaic (PV) panels	
$N_{P\text{-}B}$	Number of photovoltaic (PV) panels per branch	
$N_{P\text{-}Bsec}$	Number of photovoltaic (PV) panels per branch section	
$N_{B\text{-}L/R}$	Number of branches on the left or right of the solar tower	
$N_{B\text{-}ST}$	Number of branches on the solar tower	
N_ϕ	Number of phases	
N_{ST}	Number of solar towers	
N_{day}	Day number in a year from 1 to 365	
P	Absolute pressure	(Pa)
$P_{ST\text{-}L/R}$	Solar tower left or right half output power	(W) or (MW)
P_{ST}	Solar tower output power	(W) or (MW)
$P_{ST\text{-}50}$	Solar tower output power (50 towers)	(W) or (MW)
P_w	Photovoltaic (PV) panel width	(m)
P_l	Photovoltaic (PV) panel length	(m)
r_{sun}	Distance from the center of the sun to the center of the earth	(m)
R	Resistor value	(Ω)
R_P, R_S	Photovoltaic (PV) device parallel resistance, series resistance	(Ω)
R_{TH}	Thevenin equivalent resistance	(Ω)
R_C	Electrolytic cell resistance	(Ω)
S_h	Solar tower structure height	(m)
S_w	Solar tower structure width	(m)
t	Time duration	
T	Absolute temperature, ITS-90 or Celsius temperature	(K) or (°C)
T_C	Surface temperature of IC package	(°C)
T_f	Fusion temperature	(K)
T_P	Time period for a cycle	
u, U	Vector, vector DC component	
$V_{NaOH(aq)}$	Aqueous sodium hydroxide volume	(Gal)
V_{ST}	Solar tower output voltage	(V)
$V_{ST\text{-}MAX}$	Solar tower maximum output voltage	(V)
$V_{ST\text{-}DROP}$	Solar tower central column conductor voltage drop	(V)
V_{IN}	DC-DC converter input voltage	(V)
V_{OUT}	DC-DC converter output voltage	(V)
V_{BAT}	Utility scale battery voltage	(V)
V_{CELL}	Electrolytic cell voltage	(V)
V_{OC}	Photovoltaic (PV) panel open circuit voltage	(V)
$V_{MPP\text{-}C}$	Photovoltaic (PV) single cell maximum power point voltage	(V)

http://dx.doi.org/10.5772/67597

$V_{MPP\text{-}P}$	Photovoltaic (PV) panel maximum power point voltage	(V)
$V_{MPP\text{-}PA}$	Photovoltaic (PV) panel array maximum power point voltage	(V)
V_{TH}	Thevenin equivalent voltage	(V)
V_{CE}	IGBT collector-emitter voltage	(V)
V_{SEN}	DC-DC converter scaled input voltage	(V)
V_{SET}	DC-DC converter input voltage, set point reference	(V)
V_{ERROR}	DC-DC converter control circuit, error amplifier output	(V)
$V_{CONTROL}$	DC-DC converter control circuit, PID circuit output	(V)
w'	Precipitable water thickness at actual atmospheric pressure and temperature	(cm)
x, X	Vector, vector DC component	
α_s	Solar altitude or elevation angle above the observer's horizon	(°)
$\alpha_{s\text{-}max}$	Maximum solar altitude or elevation angle above the observer's horizon	(°)
ϕ_{Shift}	Phase shift	(°)
γ_s	Solar azimuth angle	(°)
Γ	Day angle	(radians)
η_{CELL}	Electrolytic cell efficiency	(%)
$\eta_{DC\text{-}DC}$	DC-DC converter efficiency	(%)
η_{PV}	Photovoltaic (PV) device panel efficiency	(%)
φ	Geographic latitude	(°)
λ	Geographic longitude	(°)
λ_e	Ecliptic longitude	(°)
λ_L	Local longitude	(°)
λ_S	Standard longitude	(°)
θ	Angle between position of earth in orbit around sun and perihelion position	(°)
θ_{sz}	Solar zenith angle	(°)
ρ_{plant}	Photovoltaic (PV) plant density	(mi^{-2})
τ_r	Transmittance by Rayleigh scattering	
τ_o	Transmittance by ozone	
τ_g	Transmittance by uniformly mixed gases	
τ_w	Transmittance by precipitable water vapor	
τ_a	Transmittance by aerosol	
R_g	Molar gas constant	8.3144621 (J/K·mol)
M_{air}	Molar mass, air	0.028964 (kg/mol)
R_{air}	Specific gas constant, air	287.06194 (J/K·kg)
e	Eccentricity of earth's elliptical orbit around the sun	0.01673
F	Faraday constant	96485.3365 (C/mol)
g_0	Gravitational acceleration near earth's surface	9.80665 (m/s^2)

Irr_0	Solar constant	1367 (W/m^2)
P_0	Standard atmospheric pressure	101325 (Pa)
P_{sun}	Power output of the sun	3.8×10^{26} (W)
P_{earth}	Power output of the sun reaching the earth	1.7×10^{17} (W)
R_{sun}	Radius of the sun	6.96×10^{8} (m)
$r_{sun\text{-}m}$	Mean distance from center of sun to center of earth	1.496×10^{11} (m)
T_0	Celsius zero point, ITS-90	273.15 (K)
T_{Eu}	Eutectic temperature of NaCl-H_2O solution	−21.2 (°C)
T_{sun}	Surface temperature of the solar black body	5800 (K)
T_{es}	Period of earth's rotation around the sun	365.24 (days)
T_{ea}	Period of earth's rotation on its axis (*mean solar day*)	86,400 (sec)
ε	Obliquity or tilt angle of earth's rotation axis	23.44 (°)
δ	Solar angle of declination	$-23.44 \le \delta \le +23.44$ (°)
η_{PVmax}	Thermodynamic efficiency limit of PV device panels	93 (%)
$\varphi_{T\text{-}CAN}$	Latitude at Tropic of Cancer	+23.44 (°)
$\varphi_{T\text{-}CAP}$	Latitude at Tropic of Capricorn	−23.44 (°)
λ_{PM}	Longitude at Greenwich Prime Meridian	0 (°)
π	Number, pi	3.14
ω_{ea}	Angular velocity of earth's rotation on its axis	7.292115×10^{-5} (rad/sec)

Author details

Alvin G. Stern

Address all correspondence to: inquiries@agstern.com

AG STERN, LLC, Newton, MA, USA

References

[1] Lutz, W., Samir, K.C., "Dimensions of global population projections: what do we know about future population trends and structures?," Philosophical Transactions of the Royal Society of London B: Biological Sciences, 365(1554), 2779–2791, (2010).

[2] Cohen, J.E., "Human Population: The Next Half Century," Science, 302(5648), 1172–1175, (2003).

[3] Cohen, J.E., "Population Growth and Earth's Human Carrying Capacity," Science, 269 (5222), 341–346, (1995).

[4] Narayan, P.K., Smyth, R., "Energy consumption and real GDP in G7 countries: New evidence from panel cointegration with structural breaks," Energy Economics, 30(5), 2331–2341, (2008).

[5] Soytas, U., Sari, R., "Energy consumption and income in G-7 countries," Journal of Policy Modeling, 28(7), 739–750, (2006).

[6] Stern, D.I., "Energy and economic growth in the USA: A multivariate approach," Energy Economics, 15(2), 137–150, (1993).

[7] Dignon, J., "NO_X and SO_X emissions from fossil fuels: A global distribution," Atmospheric Environment. Part A. General Topics, 26(6), 1157–1163, (1992).

[8] Gustafsson, Ö., Krusa, M., Zencak, Z., Sheesley, R.J., Granat, L., Engström, E., Praveen, P.S., Rao, P.S.P., Leck, C., Rodhe, H., "Brown Clouds over South Asia: Biomass or Fossil Fuel Combustion?," Science, 323(5913), 495–498, (2009).

[9] Mukhopadhyay, K., Forssell, O., "An empirical investigation of air pollution from fossil fuel combustion and its impact on health in India during 1973–1974 to 1996–1997," Ecological Economics, 55(2), 235–250, (2005).

[10] Streets, D.G., Waldhoff, S.T., "Present and future emissions of air pollutants in China: SO_2, NO_X, and CO," Atmospheric Environment, 34(3), 363–374, (2000).

[11] Reddy, M.S., Venkataraman, C., "Inventory of aerosol and sulphur dioxide emissions from India: I-Fossil fuel combustion," Atmospheric Environment, 36(4), 677–697, (2002).

[12] Chakraborty, N., Mukherjee, I., Santra, A.K., Chowdhury, S., Chakraborty, S., Bhattacharya, S., Mitra, A.P., Sharma, C., "Measurement of CO_2, CO, SO_2, and NO emissions from coal-based thermal power plants in India," Atmospheric Environment, 42(6), 1073–1082, (2008).

[13] Chan, C.C., "The State of the Art of Electric, Hybrid, and Fuel Cell Vehicles," Proceedings of the IEEE, 95(4), 704–718, (2007).

[14] Romm, J., "The car and fuel of the future," Energy Policy, 34(17), 2609–2614, (2006).

[15] Rotering, N., Ilic, M., "Optimal Charge Control of Plug-In Hybrid Electric Vehicles in Deregulated Electricity Markets," IEEE Transactions on Power Systems, 26(3), 1021–1029, (2011).

[16] Hoffmann, B.S., Szklo, A., "Integrated gasification combined cycle and carbon capture: A risky option to mitigate CO_2 emissions of coal-fired power plants," Applied Energy, 88(11), 3917–3929, (2011).

[17] Sims, R.E.H., Rogner, H.H., Gregory, K., "Carbon emission and mitigation cost comparisons between fossil fuel, nuclear and renewable energy resources for electricity generation," Energy Policy, 31(13), 1315–1326, (2003).

[18] Rosen, M.A., "Energy- and exergy-based comparison of coal-fired and nuclear steam power plants," Exergy, An International Journal, 1(3), 180–192, (2001).

[19] Benke, A.C., "A Perspective on America's Vanishing Streams," Journal of the North American Benthological Society, 9(1), 77–88, (1990).

[20] Kosnik, L., "The potential for small scale hydropower development in the US," Energy Policy, 38(10), 5512–5519, (2010).

[21] Eberle, U., Müller, B., von Helmolt, R., "Fuel cell electric vehicles and hydrogen infrastructure: status 2012," Energy & Environmental Science, 5(10), 8780–8798, (2012).

[22] von Helmolt, R., Eberle, U., "Fuel cell vehicles: Status 2007," Journal of Power Sources, 165(2), 833–843, (2007).

[23] Kordesch, K.V., "Hydrogen-Air/Lead Battery Hybrid System for Vehicle Propulsion," Journal of The Electrochemical Society, 118(5), 812–817, (1971).

[24] Bagotsky, V.S., Fuel Cells: Problems and Solutions. Hoboken, NJ: John Wiley & Sons, pp. 7–70, 109–123, 189–239, (2009).

[25] Eberle, U., von Helmolt, R., "Sustainable transportation based on electric vehicle concepts: a brief overview," Energy & Environmental Science, 3(6), 689–699, (2010).

[26] Paster, M.D., Ahluwalia, R.K., Berry, G., Elgowainy, A., Lasher, S., McKenney, K., Gardiner, M., "Hydrogen storage technology options for fuel cell vehicles: Well-to-wheel costs, energy efficiencies, and greenhouse gas emissions," International Journal of Hydrogen Energy, 36(22), 14534–14551, (2011).

[27] Schüth, F., Bogdanovic, B., Felderhoff, M., "Light metal hydrides and complex hydrides for hydrogen storage," Chemical Communications, 20, 2249–2258, (2004).

[28] Zaluski, L., Zaluska, A., Ström-Olsen, J.O., "Hydrogenation properties of complex alkali metal hydrides fabricated by mechano-chemical synthesis," Journal of Alloys and Compounds, 290(1–2), 71–78, (1999).

[29] Bogdanovic, B., Schwickardi, M., "Ti-doped alkali metal aluminum hydrides as potential novel reversible hydrogen storage materials," Journal of Alloys and Compounds, 253–254, 1–9, (1997).

[30] Zhang, Y., Liao, S., Xu, Y., "Highly active alkali metal hydrides; their catalytic syntheses and properties," Journal of Molecular Catalysis, 84(3), 211–221, (1993).

[31] Knowlton, R.E., "An investigation of the safety aspects in the use of hydrogen as a ground transportation fuel," International Journal of Hydrogen Energy, 9(1–2), 129–136, (1984).

[32] Hord, J., "Is hydrogen a safe fuel?," International Journal of Hydrogen Energy, 3(2), 157–176, (1978).

[33] Brown, L.F., "A comparative study of fuels for on-board hydrogen production for fuel-cell-powered automobiles," International Journal of Hydrogen Energy, 26(4), 381–397, (2001).

[34] Xu, J., Froment, G.F., "Methane Steam Reforming, Methanation and Water-Gas Shift: I. Intrinsic Kinetics," AlChE Journal, 35(1), 88–96, (1989).

[35] Baschuk, J.J., Li, X., "Carbon monoxide poisoning of proton exchange membrane fuel cells," International Journal of Energy Research, 25(8), 695–713, (2001).

[36] Si, Y., Jiang, R., Lin, J.C., Kunz, H.R., Fenton, J.M., "CO Tolerance of Carbon-Supported Platinum-Ruthenium Catalyst at Elevated Temperature and Atmospheric Pressure in a PEM Fuel Cell," Journal of The Electrochemical Society, 151(11), A1820–A1824, (2004).

[37] Stern, A.G., "Design of an efficient, high purity hydrogen generation apparatus and method for a sustainable, closed clean energy cycle," International Journal of Hydrogen Energy, 40(32), 9885–9906, (2015).

[38] Bodnar, R.J., "Revised equation and table for determining the freezing point depression of H_2O-NaCl solutions," Geochimica et Cosmochimica Acta, 57(3), 683–684, (1993).

[39] Hall, D.L., Sterner, S.M., Bodnar, R.J., "Freezing point Depression of NaCl-KCl-H_2O Solutions," Economic Geology, 83(1), 197–202, (1988).

[40] Castner, H.Y., "Process of manufacturing sodium and potassium," U.S. Patent 452,030, (1891).

[41] Downs, J.C., "Electrolytic process and cell," U.S. Patent 1,501,756, (1924).

[42] Davy, H., "The Bakerian Lecture: On Some New Phenomena of Chemical Changes Produced by Electricity, Particularly the Decomposition of the Fixed Alkalies, and the Exhibition of the New Substances Which Constitute Their Bases; And on the General Nature of Alkaline Bodies" Philosophical Transactions of the Royal Society of London, 98, 1–44, (1808).

[43] Weast, R.C., Handbook of Chemistry and Physics. Cleveland, OH: CRC Press, pp. F13, F104, F242, D141–D146, (1976–1977).

[44] Daly, C., Halbleib, M., Smith, J.I., Gibson, W.P., Doggett, M.K., Taylor, G.H., Curtis, J., Pasteris, P.P., "Physiographically sensitive mapping of climatological temperature and precipitation across the conterminous United States," International Journal of Climatology, 28(15), 2031–2064, (2008).

[45] Wilson, G.H., "The Hottest Region in the United States," Monthly Weather Review, 43 (6), 278–280, (1915).

[46] Court, A., "How Hot is Death Valley?," Geographical Review, 39(2), 214–220, (1949).

[47] Fthenakis, V., Mason, J.E., Zweibel, K., "The technical, geographical, and economic feasibility for solar energy to supply the energy needs of the US," Energy Policy, 37(2), 387–399, (2009).

[48] Renewable Resource Data Center, The National Solar Radiation Data Base (NSRDB), National Renewable Energy Laboratory, Golden, CO. U.S.A.

[49] Frosch, R.A., Gallopoulos, N.E., "Strategies for Manufacturing," Scientific American, 261(3), 144–152, (1989).

[50] Henry, C.H., "Limiting efficiencies of ideal single and multiple energy gap terrestrial solar cells," Journal of Applied Physics, 51(8), 4494–4500, (1980).

[51] Press, W.H., "Theoretical maximum for energy from direct and diffuse sunlight," Nature, 264, 734–735, (1976).

[52] Shockley, W., Queisser, H.J., "Detailed Balance Limit of Efficiency of p-n Junction Solar Cells," Journal of Applied Physics, 32(3), 510–519, (1961).

[53] Bagnall, D.M., Boreland, M., "Photovoltaic technologies," Energy Policy, 36(12), 4390–4396, (2008).

[54] Stern, A.G., "Design of high quantum efficiency and high resolution, Si/SiGe avalanche photodiode focal plane arrays using novel, back-illuminated, silicon-on-sapphire substrates," in Park, J.W., Editor. Photodiodes – World Activities in 2011. Vienna: InTech Publisher, pp. 267–312, ISBN 978-953-307-530-3, (2011).

[55] Stern, A.G., "Design of a high sensitivity emitter-detector avalanche photodiode imager using very high transmittance, back-illuminated, silicon-on-sapphire," SPIE Journal of Optical Engineering, 51(6), 063206, (2012).

[56] Stern, A.G., "Very high transmittance, back-illuminated, silicon-on-sapphire semiconductor wafer substrate for high quantum efficiency and high resolution, solid-state, imaging focal plane arrays," U.S. Patent 8,354,282, (2013).

[57] Stern, A.G., "Thin, very high transmittance, back-illuminated, silicon-on-sapphire semiconductor substrates bonded to fused silica," U.S. Patent 8,471,350, (2013).

[58] Sadok, M., Benyoucef, B., Benmedjahed, M., "Assessment of PV Modules Degradation based on Performances and Visual Inspection in Algerian Sahara," International Journal of Renewable Energy Research, 6(1), 106–116, (2016).

[59] Garg, H.P., Treatise on Solar Energy: Fundamentals of Solar Energy, Volume 1. New York: John Wiley & Sons, pp. 50–150, (1982).

[60] Sproul, A.B., "Derivation of the solar geometric relationships using vector analysis," Renewable Energy, 32(7), 1187–1205, (2007).

[61] Kalogirou, S.A., Solar Energy Engineering, Processes and Systems, 2nd edition. Waltham, MA: Academic Press, pp. 51–122, (2014).

[62] Guinot, B., Seidelmann, P.K., "Time scales: their history, definition and interpretation," Astronomy and Astrophysics, 194(1–2), 304–308, (1988).

[63] Essen, L., "Time Scales," Metrologia, 4(4), 161–165, (1968).

[64] Aoki, S., Guinot, B., Kaplan, G.H., Kinoshita, H., McCarthy, D.D., Seidelmann, P.K., "The New Definition of Universal Time," Astronomy and Astrophysics, 105(2), 359–361, (1982).

[65] Capitaine, N., Gontier, A.M., "Accurate procedure for deriving UT1 at a submilliarcsecond accuracy from Greenwich Sidereal Time or from the stellar angle," Astronomy and Astrophysics, 275, 645–650, (1993).

[66] Capitaine, N., Wallace, P.T., McCarthy, D.D., "Expressions to implement the IAU 2000 definition of UT1," Astronomy and Astrophysics, 406(3), 1135–1149, (2003).

[67] Moritz, H., "Geodetic reference system 1980," Journal of Geodesy, 54(3), 395–405, (1980).

[68] Malys, S., Seago, J.H., Pavlis, N.K., Seidelmann, P.K., Kaplan, G.H., "Why the Greenwich meridian moved," Journal of Geodesy, 89(12), 1263–1272, (2015).

[69] Spencer, J.W., "Fourier series representation of the position of the sun," Search, 2(5), 172, (1971).

[70] Hughes, D.W., Yallop, B.D., Hohenkerk, C.Y., "The Equation of Time," Monthly Notices of the Royal Astronomical Society, 238(4), 1529–1535, (1989).

[71] Grena, R., "Five new algorithms for the computation of sun position from 2010 to 2110," 86(5), 1323–1337, (2012).

[72] Grena, R., "An algorithm for the computation of the solar position," Solar Energy, 82(5), 462–470, (2008).

[73] Reda, I., Andreas, A., "Solar position algorithm for solar radiation applications," Solar Energy, 76(5), 577–589, (2004).

[74] Reda, I., Andreas, A., "Solar Position Algorithm for Solar Radiation Applications," NREL/TP-560-34302. Golden, CO: National Renewable Energy Laboratory, (2008).

[75] Blanco-Muriel, M., Alarcón-Padilla, D.C., López-Moratalla, T., Lara-Coira, M., "Computing the solar vector," Solar Energy, 70(5), 431–441, (2001).

[76] Michalsky, J.J., "*The Astronomical Almanac's* algorithm for approximate solar position (1950–2050)," Solar Energy, 40(3), 227–235, (1988).

[77] Young, A.T., "Air mass and refraction," Applied Optics, 33(6), 1108–1110, (1994).

[78] Iqbal, M., An Introduction to Solar Radiation. New York, NY: Academic Press, pp. 85–212, (1983).

[79] Bird, R., Hulstrom, R.L., "Direct Insolation Models," SERI/TR-335-344. Golden, CO: Solar Energy Research Institute, (1980).

[80] Bird, R., Hulstrom, R.L., "A Simplified Clear Sky Model for Direct and Diffuse Insolation on Horizontal Surfaces," SERI/TR-642-761. Golden, CO: Solar Energy Research Institute, (1981).

[81] Taylor, B.N., Thompson, A., "The International System of Units (SI)," NIST Special Publication 330. Gaithersburg, MD: National Institute of Standards and Technology, (2008).

[82] Mohr, P.J., Taylor, B.N., Newell, D.B., "CODATA recommended values of the fundamental physical constants: 2010," Reviews of Modern Physics, 84(4), 1527–1605, (2012).

[83] Mitchell, T.D., Carter, T.R., Jones, P.D., Hulme, M., New, M., "A comprehensive set of high-resolution grids of monthly climate for Europe and the globe: the observed record (1901–2000) and 16 scenarios (2001–2100). (CRU TS 2.0)," Tyndall Centre Working Paper 55, Climatic Research Unit, School of Environmental Sciences, University of East Anglia, pp. 1–25, (2004).

[84] Randel, D.L., Vonder Haar, T.H., Ringerud, M.A., Stephens, G.L., Greenwald, T.J., Combs, C.L., "A New Global Water Vapor Dataset," Bulletin of the American Meteorological Society, 77(6), 1233–1246, (1996).

[85] Tuller, S.E., "World Distribution of Mean Monthly and Annual Precipitable Water," Monthly Weather Review, 96(11), 785–797, (1968).

[86] Phokate, S., Pisutthipong, N., "The Transmittance to Direct Irradiance due to Absorption by Precipitable Water Vapor in the Atmosphere," Advanced Materials Research, 979, 7–10, (2014).

[87] Phokate, S., "The Distribution of Precipitable Water Vapor in the Atmosphere of Thailand," In Proceeding of 4th International Science, Social Science, Engineering and Energy Conference (I-SEEC), Petchburi, Thailand, pp. 558–563, (2013).

[88] Peel, M.C., Finlayson, B.L., McMahon, T.A., "Updated world map of the Köppen-Geiger climate classification," Hydrology and Earth System Sciences, 11(5), 1633–1644, (2007).

[89] Winslow, J.C., Hunt, E.R., Piper, S.C., "A globally applicable model of daily solar irradiance estimated from air temperature and precipitation data," Ecological Modelling, 143 (3), 227–243, (2001).

[90] Jeffrey, S.J., Carter, J.O., Moodie, K.B., Beswick, A.R., "Using spatial interpolation to construct a comprehensive archive of Australian climate data," Environmental Modelling & Software, 16(4), 309–330, (2001).

[91] Liu, D.L., Scott, B.J., "Estimation of solar radiation in Australia from rainfall and temperature observations," Agricultural and Forest Meteorology, 106(1), 41–59, (2001).

[92] Maddox R.A., McCollum, D.M., Howard, K.W., "Large-Scale Patterns Associated with Severe Summertime Thunderstorms over Central Arizona," Weather and Forecasting, 10(4), 763–778, (1995).

[93] Blanchard, D.O., "A Comparison of Wind Speed and Forest Damage Associated with Tornadoes in Northern Arizona," Weather and Forecasting, 28(2), 408–417, (2013).

[94] Villalva, M.G., Filho, E.R., "Dynamic analysis of the input-controlled buck converter fed by a photovoltaic array," SBA: Controle & Automação Sociedade Brasileira de Automatica, 19(4), 463–474, (2008).

[95] Gao, L., Dougal, R.A., Liu, S., Iotova, A.P., "Parallel-Connected Solar PV System to Address Partial and Rapidly Fluctuating Shadow Conditions," IEEE Transactions on Industrial Electronics, 56(5), 1548–1556, (2009).

[96] Bidram, A., Davoudi, A., Balog, R.S., "Control and Circuit Techniques to Mitigate Partial Shading Effects in Photovoltaic Arrays," IEEE Journal of Photovoltaics, 2(4), 532–546, (2012).

[97] Patel, H., Agarwal, V., "MATLAB-Based Modeling to Study the Effects of Partial Shading on PV Array Characteristics," IEEE Transactions on Energy Conversion, 23(1), 302–310, (2008).

[98] IEC standard voltages, IEC 60038 Edition 6.2, International Electrotechnical Commission (IEC), (1983).

[99] Hine, F., "Fused Salt Electrolysis and Electrothermics," in Electrode Processes and Electrochemical Engineering, New York, NY: Plenum Press, pp. 193–217, (1985).

[100] Mazumder, S.K., "Stability Analysis of Parallel DC-DC Converters," IEEE Transactions on Aerospace and Electronic Systems, 42(1), 50–69, (2006).

[101] Middlebrook, R.D., Cuk, S., "A general unified approach to modeling switching-converter power stages," International Journal of Electronics, 42(6), 521–550, (1977).

[102] Gurvich, L.V., Bergman, G.A., Gorokhov, L.N., Iorish, V.S., Leonidov, V.Ya., Yungman, V. S., "Thermodynamic Properties of Alkali Metal Hydroxides. Part 1. Lithium and Sodium Hydroxides," Journal of Physical and Chemical Reference Data, 25(4), 1211–1276, (1996).

[103] Millero, F.J., Feistel, R., Wright, D.G., McDougall, T.J., "The composition of Standard Seawater and the definition of the Reference-Composition Salinity Scale," Deep-Sea Research Part I: Oceanographic Research Papers, 55(1), 50–72, (2008).

[104] Bureau of Transportation Statistics, U.S. Department of Transportation, Southeast Washington, DC. U.S.A.

IntechOpen